PRINT-92-0205
Fermilab Library
0 1160 0013424 1

The Power Spectrum of IRAS Galaxies[1]

Karl B. Fisher

Physics and Astronomy Departments, University of California

Berkeley, California 94720

Marc Davis

Physics and Astronomy Departments, University of California

Berkeley, California 94720

Michael A. Strauss

Institute for Advanced Study, School of Natural Sciences

Princeton, New Jersey 08540

Amos Yahil

Astronomy Program, State University of New York

ESS Building, Stony Brook, New York 11794-2100

and

Institut D'Astrophysique, 98 bis,

Boulevard Arago, 75014, Paris, FRANCE

John P. Huchra

Center for Astrophysics, 60 Garden Street

Cambridge, Massachusetts 02138

ROUTE TO
NAME | LOCATION
RETURN TO FERMI LIBRARY

Accepted for Publication in the Astrophysical Journal

JUN 2 1992

[1] Based in part on data obtained at Lick Observatory, operated by the University of California; the Multiple Mirror Telescope, a joint facility of the Smithsonian Astrophysical Observatory and the University of Arizona; and Cerro Tololo Inter-American Observatory; operated by the Association of Universities for Research in Astronomy, Inc., under contract with the National Science Foundation.

ABSTRACT

We have computed the power spectrum of galaxy clustering, $P(k)$, for a flux-limited redshift survey of 5304 galaxies detected by the *Infrared Astronomical Satellite* (*IRAS*), using a window function which minimizes the aliasing due to the sample boundaries. We use Monte-Carlo realizations of the data sample drawn from an N-body simulation of a Cold Dark Matter (CDM) universe to check our methods and to derive error estimates for the *IRAS* power spectrum. The derived *IRAS* $P(k)$ appears consistent with the known two-point correlation function of *IRAS* galaxies on scales $\sim 20\ h^{-1}$Mpc extrapolated out to large spatial scales ($2\pi/k \lesssim 100\ h^{-1}$Mpc) and is characterized by a power law, $P(k) \propto k^n$, with $n \sim -1.4$. On larger scales, the *IRAS* power spectrum begins to flatten, but we see no significant evidence for a turnover out to the largest scales we measure, $\sim 180\ h^{-1}$Mpc.

We compare the *IRAS* power spectrum qualitatively with a variety of theoretical models. The shape of the *IRAS* power spectrum is not well matched by the standard CDM model ($\Omega h = 0.5$); models with more large scale power such as CDM with $\Omega h = 0.2$ or CDM seeded with textures provide a better fit to the *IRAS* power spectrum. We perform a detailed quantitative comparison between standard CDM and the data using N-body simulations to map out the error distribution of $P(k)$ on large scales.

We find that the variance in the measured power on the largest scales is dominated by the poor sampling of Fourier modes with wavelengths comparable to the size of the sample, rather than by dilute sampling statistics. Consequently, in order to determine the validity of the standard CDM model on large scales, one must analyze many *independent* realizations of the CDM power spectrum. The analysis of repeated sampling of a single realization results in a significant underestimation of the variance in the CDM power which can lead to incorrect conclusions regarding the statistical significance of an observed power spectrum.

The large sky coverage of our survey and our choice of window function leads to the orthogonality of different modes. We use this fact, in addition to the assumption of linear biasing, to derive the probability that the standard CDM model can produce power of comparable amplitude to that measured in the *IRAS* sample on large scales. On scales between 36 h^{-1}Mpc and 180 h^{-1}Mpc, consistency of the CDM model with the *IRAS* data constrains the linear biasing parameter, b, (*IRAS* to dark matter) to be $b < 1.5$ at the 95% confidence level and $b < 2$ at the 99% confidence level. On large scales the CDM model is in good agreement with the *IRAS* $P(k)$ if *IRAS* galaxies are unbiased tracers of the mass distribution (b=1). However, if the linear biasing model were to extend to smaller scales, it would lead to excessive power.

1. Introduction

The two-point correlation function, $\xi(r)$, has traditionally been the primary statistic used to quantify galaxy clustering observationally. Measurements of $\xi(r)$ from existing redshift surveys on spatial scales that are undergoing non-linear evolution (i.e., where $\xi(r) >> 1$) have proven to be quite robust and reproducible. The canonical correlation function for optically selected galaxies is a power-law, $\xi(r) = (r/5.4h^{-1}\mathrm{Mpc})^{-1.8}$, for $r \lesssim 15\ h^{-1}\mathrm{Mpc}$ (Davis & Peebles 1983; cf., de Lapparent, Geller, & Huchra 1988), where the Hubble Constant is given by $H_0 = 100\ h$ km s^{-1} Mpc^{-1}. Galaxies selected from the database of the *Infrared Astronomical Satellite* (*IRAS*) are characterized by a somewhat smaller correlation length and shallower slope with $\xi(r) = (r/3.79h^{-1}\mathrm{Mpc})^{-1.57}$ (Saunders, Rowan-Robinson, & Lawrence 1992; Strauss *et al.* 1992a).

In linear theory, the shape of the correlation function is maintained during the growth of the perturbations, and a current measurement of $\xi(r)$ in the region $\xi(r) << 1$ would yield the intial power spectrum. But this is exactly where $\xi(r)$ is most difficult to determine observationally. Since $1 + \xi(r)$ is calculated from a redshift survey by dividing the pair counts at a separation r by a quantity proportional to the mean density of the survey n, the uncertainty in $\xi(r)$ for $\xi(r) \lesssim 1$ will be limited by the fractional uncertainty in the mean density, $\Delta\xi \simeq \Delta n/n$. The uncertainty in n is due both to random errors arising from small number statistics, and to systematic effects caused by fluctuations on the size of the sample (Davis & Huchra 1982; Efstathiou, Ellis, & Peterson 1988), uncertainties in the degree of galaxy evolution (Fisher *et al.* 1992), errors in the selection function $\phi(r)$, and the neglect of relativistic corrections to the volume element. At best, current redshift surveys can determine the mean density to within $\approx 5\%$, making it very difficult to directly determine the correlation function on scales $\gtrsim 30\ h^{-1}\mathrm{Mpc}$.

The power spectrum of fluctuations $P(k)$ is simply the Fourier conjugate of the correlation function. There have been a number of recent determinations of $P(k)$ from redshift surveys (Baumgart & Fry 1991; Einasto & Gramann 1991; Kaiser 1991; Hamilton *et al.* 1991; Peacock & Nicholson 1991; Peacock 1991; Park, Gott, & da Costa 1992; Vogeley *et al.* 1992). The power spectrum can be more accurately determined in the presence of uncertainties in the mean density than can $\xi(r)$; as we shall see in Equation 2 below, for scales much smaller than the sample size, where the effects of the sample edges are unimportant, the calculated power spectrum is proportional to n^{-2}. Thus an error in the mean density of the sample only alters the normalization of the power spectrum without changing its shape. Because no theoretical models for the power spectrum currently predict the normalization *a priori*, but rather are normalized from the observations, this uncertainty in the normalization is of little consequence in comparing the results with the models.

There are recent indications that the power spectrum predicted by the standard Cold Dark Matter (CDM) model with $\Omega h = 0.5$ is too flat for wavenumbers corresponding to spatial scales $r \gtrsim 50\ h^{-1}$Mpc; equivalently, when normalized to observed galaxy fluctuations on small scales, CDM has insufficient power on large scales (see also Bertschinger & Juszkiewicz 1988; Efstathiou, Sutherland, & Maddox 1990*a*; Maddox *et al.* 1990; Park 1991). In this paper, we compute the power spectrum from a flux-limited redshift survey of 5304 *IRAS* galaxies (Fisher 1992) covering 87.6% of the sky. This is currently the largest full-sky redshift catalog in existence; the large volume of space probed by the survey combined with its simple geometry and high sampling density make it ideal for the determination of the power spectrum on large scales. Our method for extracting the power spectrum avoids using a Fast Fourier Transform (FFT) algorithm on volume limited subsamples; instead, the Fourier transform is performed as a direct point transform on the full flux-limited catalog. We find that the *IRAS* $P(k)$ measured in redshift space is indeed steeper than the standard CDM prediction on large scales, and is well described by a power law, $P(k) \propto k^n$, with $n \sim -1.4$ for $2\pi/k \lesssim 100\ h^{-1}$Mpc. At scales $\gtrsim 100\ h^{-1}$Mpc, the *IRAS* power spectrum begins to flatten, but the errors on this large scale are very large.

We describe our technique for extracting the power spectrum directly from flux-limited catalogs in §2. In §3, we test our technique using Monte-Carlo simulations of the *IRAS* survey based on N-body realizations of a standard CDM universe. In §4, we apply our technique to the 1.2 Jy *IRAS* catalog. We compare the resulting *IRAS* power spectrum with previous results in the literature in §5. In §6 we give a qualitative comparison of the *IRAS* power spectrum with various theoretical models. §7 describes an extensive set of Monte-Carlo experiments designed to quantitatively test the validity of standard CDM on large scales. We conclude in §8.

2. Estimating the Power Spectrum

2.1. Technique

Flux-limited galaxy catalogs are characterized by a radial selection function, $\phi(r)$, such that for a homogeneous distribution of galaxies, the expected number of galaxies in the sample on a radial shell of thickness Δr at a distance r is given by $\omega n r^2 \Delta r \phi(r)$, where n is the mean density of the entire sample and ω is its solid angle (e.g., Yahil *et al.* 1991). In a flux-limited sample, an unbiased estimator for the galaxian density contrast, $\delta(\mathbf{r}) \equiv (\rho(\mathbf{r}) - \langle\rho\rangle)/\langle\rho\rangle$, in a volume V containing galaxies at positions $\mathbf{r}_i$ is given by

$$\hat{\delta}(\mathbf{r}) = \frac{1}{n}\sum_i \frac{\delta^{(3)}(\mathbf{r}-\mathbf{r}_i)}{\phi(r_i)} - 1 \quad , \tag{1}$$

where the caret denotes the statistical estimate of a quantity. This estimate of the density field can be decomposed into a superposition of plane waves,

$$\hat{\delta}_{\mathbf{k}} = \frac{1}{nV} \sum_i \frac{1}{\phi(r_i)} e^{i\mathbf{k}\cdot\mathbf{r}_i} - W(\mathbf{k}) \quad , \tag{2}$$

where

$$W(\mathbf{k}) \equiv \frac{1}{V} \int_V d^3\mathbf{r}\, e^{i\mathbf{k}\cdot\mathbf{r}} \quad , \tag{3}$$

is the Fourier transform of the catalog window. As an estimate of the power spectrum, one can compute the square of the modulus of the Fourier amplitudes:

$$\begin{aligned} \Pi(\mathbf{k}) &\equiv \hat{\delta}_{\mathbf{k}}\, \hat{\delta}^*_{\mathbf{k}} \\ &= \frac{1}{(nV)^2} \left(\sum_i \frac{1}{\phi(r_i)} e^{i\mathbf{k}\cdot\mathbf{r}_i} - nV\, W(\mathbf{k}) \right) \left(\sum_j \frac{1}{\phi(r_j)} e^{-i\mathbf{k}\cdot\mathbf{r}_j} - nV\, W^*(\mathbf{k}) \right) \quad . \end{aligned} \tag{4}$$

The connection between $\Pi(\mathbf{k})$ and the underlying power spectrum, $P(k)$, is established by calculating the ensemble mean of $\Pi(\mathbf{k})$, denoted by $\langle \Pi(\mathbf{k}) \rangle$. The expectation values of the sums appearing in Equation 4 can be converted into integrals by rewriting the direct summation over particles as sums over infinitesimal cells with volumes $d^3\mathbf{r}_i$ and occupation numbers N_i (cf., Peebles 1980 §41.1),

$$\begin{aligned} \langle \Pi(\mathbf{k}) \rangle = &\frac{1}{(nV)^2} \sum_{cells\ i,j} \frac{\langle N_i N_j \rangle}{\phi(r_i)\phi(r_j)} e^{i\mathbf{k}\cdot(\mathbf{r}_i - \mathbf{r}_j)} + |W(\mathbf{k})|^2 \\ &- \frac{1}{nV} \sum_{cells\ i} \frac{\langle N_i \rangle}{\phi(r_i)} \left[W(\mathbf{k}) e^{-i\mathbf{k}\cdot\mathbf{r}_i} + W^*(\mathbf{k}) e^{i\mathbf{k}\cdot\mathbf{r}_i} \right] \quad . \end{aligned} \tag{5}$$

The mean value of the occupation number for a cell located at radius r, is given by the expected count in a homogeneous universe, $n\phi(r)d^3\mathbf{r}$. The second moment of the counts is given by

$$\langle N_i N_j \rangle = \begin{cases} n^2(1 + \xi(|\mathbf{r}_i - \mathbf{r}_j|))\phi(r_i)\phi(r_j) d^3\mathbf{r}_i d^3\mathbf{r}_j, & i \neq j \\ n\phi(r_i) d^3\mathbf{r}_i, & i = j \end{cases} \quad . \tag{6}$$

In the case $i = j$, we have used the fact that for infinitesimal cells, N_i can only take on the values 0 and 1, and thus $\langle N_i^2 \rangle = \langle N_i \rangle$.

Substituting Equation 6 into Equation 5 yields the expectation value of the estimator $\Pi(\mathbf{k})$,

$$\langle \Pi(\mathbf{k}) \rangle = \frac{1}{V^2} \int d^3\mathbf{r}_1 d^3\mathbf{r}_2 \xi(r_{12}) e^{i\mathbf{k}\cdot\mathbf{r}_{12}} + \frac{1}{nV^2} \int d^3\mathbf{r} \frac{1}{\phi(r)} \quad . \tag{7}$$

We can recast Equation 7 in terms of the true power spectrum by recalling that $\xi(r)$ is the Fourier conjugate of $P(k)$. Here and throughout, the Fourier transforms will be defined by the following convention:

$$\begin{aligned} \xi(r) &= \frac{1}{(2\pi)^3} \int d^3\mathbf{k}\ P(k) e^{-i\mathbf{k}\cdot\mathbf{r}} \\ P(k) &= \int d^3\mathbf{r}\ \xi(r) e^{+i\mathbf{k}\cdot\mathbf{r}} \quad . \end{aligned} \tag{8}$$

In this convention, $P(k)$ is a spectral density and thus has the units of volume. One often sees this Fourier transform pair presented with a volume term normalizing the integrals, so as to make $P(k)$ dimensionless. This has the undesirable effect of making $P(k)$ dependent on the volume in which it is defined.

Expressing $\xi(r)$ in terms of $P(k)$ in Equation 7 gives

$$\langle \Pi(\mathbf{k}) \rangle = \frac{\tilde{P}(\mathbf{k})}{V} + \frac{1}{nV^2} \int d^3\mathbf{r} \frac{1}{\phi(r)} \quad , \tag{9a}$$

where

$$\tilde{P}(\mathbf{k}) \equiv \int d^3\mathbf{k}' \, P(k') G(\mathbf{k} - \mathbf{k}') \tag{9b}$$

with

$$G(\mathbf{k} - \mathbf{k}') \equiv \frac{V}{(2\pi)^3} |W(\mathbf{k} - \mathbf{k}')|^2 \quad . \tag{9c}$$

Thus the mean value of the estimator, $\Pi(k)$, is simply the true power spectrum convolved with a window function that describes the geometry of the sample, plus an additional shot noise term. By isotropy, the mean value of $\Pi(\mathbf{k})$ is a function of the magnitude of $\mathbf{k}$ only. In practice, one must average the expression given in Equation 4 over wavenumbers of fixed $|\mathbf{k}|$ but with random directions in k-space.

The shot noise term in Equation 9a is the generalization of the usual Poisson discreteness term $1/nV$ for a sample characterized by a radial selection function; in the presence of non-uniform radial weighting the Poisson term is multiplied by the volume-averaged weight $\frac{1}{V} \int \frac{d^3\mathbf{r}}{\phi(r)}$. The shot noise term in Equation 9a is the expectation value; in a given realization the shot noise is given exactly by the sum

$$\frac{1}{(nV)^2} \sum_i \frac{1}{\phi^2(r_i)} \quad . \tag{10}$$

The convolution in Equation 9b is a manifestation of the uncertainty principle. Because the density is sampled in a finite volume, there is an inherent resolution limit Δk in the power spectrum, on the order of the fundamental mode, and there is therefore no point in sampling the power spectrum more densely. For example, the window function for a spherical volume of radius R can be calculated directly from Equation 2:

$$W(\mathbf{k}) = \frac{3\, j_1(kR)}{kR} \quad , \tag{11}$$

where $j_1(x)$ is the usual spherical Bessel function.

The exact wavenumbers chosen for the estimation of the power spectrum, as well as the sampling geometry, are a matter of convenience dictated by the statistical and systematic limitations of the data, and are discussed in detail below.

Our procedure, therefore is as follows. For a given sample geometry, one averages the statistic $\Pi(\mathbf{k})$ in Equation 4 for a set of wavenumbers with fixed $|\mathbf{k}|$ but randomly distributed on a sphere in k-space. For each direction of k chosen, the shot noise given in Equation 10 is subtracted from $\Pi(\mathbf{k})$, and the result is multiplied by the sample volume; this gives an estimate for the true power spectrum convolved with an expression that depends on the sample geometry, $\tilde{P}(k)$. In the analysis that follows we average over 500 uniformly distributed directions of $\mathbf{k}$ at each frequency for which the power spectrum is computed. At this point, one could either attempt to deconvolve $\tilde{P}(k)$ and compare to theoretical predictions, or one could convolve the theoretical predictions with the appropriate kernel G, and compare directly to the measured quantity, $\tilde{P}(k)$. The latter approach is more stable, and we adopt it in this paper. Our choice of sample geometry will be discussed in the next section.

2.2. Sensitivity of $\tilde{P}(k)$ to the Mean Density and Selection Function

As a first test of the method outlined above, we laid down particles randomly within a sphere of radius R, with a radial density profile consistent with the *IRAS* selection function and number density. We then calculated the quantity $\tilde{P}(k)$ within the sphere using the methods described above, and compared it with the power spectrum $P(k) = constant$ (white noise) convolved with the window function in Equation 11 using Equation 9*b*. There was excellent agreement between the true and derived power spectrum for waves with frequencies much greater than that corresponding to the fundamental mode $k_f \sim \pi/R$. However, for frequencies close to k_f, the estimated power differed significantly from the true power.

There are three fundamental difficulties in measuring the power at low frequencies. First, from Equation 2, one expects the Fourier components of the density field to scale inversely with the density only for values of k such that $W(\mathbf{k})$ is negligible; for wavenumbers $|\mathbf{k}|$ approaching k_f, $W(\mathbf{k})$ is no longer negligible for a finite volume, and $\delta_{\mathbf{k}}$ no longer scales as n^{-1}. Consequently, errors in the determination of n cause errors in the inferred *shape* of the power spectrum on the largest scales. Second, the window function couples the Fourier modes so that they are no longer orthogonal. This coupling can become severe at large spatial scales due to the broadening of $W(\mathbf{k})$ at low frequencies, especially if one is working with irregularly shaped window functions. This covariance between modes will conspire with errors in the mean density to yield systematic errors in the estimated $P(k)$ at low frequencies.

Finally, there is the possibility of artificial large scale density gradients induced by a variety of effects. An artificial density gradient in the sample will introduce spurious power given by

$$\delta P(k) \approx \frac{1}{V}\left[\int d^3\mathbf{r}\,\Delta(\mathbf{r})e^{i\mathbf{k}\cdot\mathbf{r}}\right]^2 \quad , \tag{12}$$

where $\Delta(\mathbf{r}) = \delta n(\mathbf{r})/n(\mathbf{r})$ is the fractional error in the true density profile, $n(\mathbf{r})$. Artificial density gradients will arise from errors in the selection function and the neglect of relativistic and evolutionary effects.

For example, by working in Local Group redshift space and not correcting distances for our motion, the inferred selection function differs slightly from the true selection function that would be computed if the distances to all galaxies were known; this error in the selection function will introduce a slight radial gradient in the density. An estimate of the uncertainty of the selection function is given by the difference in the derived $\phi(r)$ when calculated in real space and redshift space for a series of N-body realizations of the *IRAS* sample (described in §3). In this case, $\Delta(\mathbf{r})$ in Equation 12 is given by $\delta\phi(r)/\phi(r)$. This results in a systematic error in $\tilde{P}(k)$ which increases with wavelength but is $\lesssim 10\%$ of the observed power for $\lambda < 180\ h^{-1}$Mpc. The problem is *not* alleviated by working with volume limited subsamples, because the determination of the absolute luminosity of each galaxy is dependent on the proper correction for the effects of peculiar motion.

To first order in distance, the fractional error in the number density introduced by the neglect of evolutionary and relativistic effects is given by

$$\Delta(r) = \frac{3}{4}\frac{rH_0}{c}\left(\alpha - 2(q_0 + 1)\right) \quad , \tag{13}$$

where α parametrizes the density evolution, $n(z) \propto (1+z)^{\alpha}$, and q_0 is the usual cosmological density parameter (Fisher *et al.* 1992). Notice that the evolutionary and relativistic corrections enter with opposite signs to first order and thus tend cancel one another for positive α. For our choice of geometry (cf., §2.3 below), $\alpha = 2$ appropriate for the 1.2 Jy *IRAS* sample (Fisher *et al.* 1992), and $q_0 = 0.5$, the error induced in the derived power spectrum by Equations 12 and 13 is $\lesssim 2\%$ on the scales probed in our analysis. If we have severely underestimated the evolution and $\alpha = 7$ (Saunders *et al.* 1990), then the error in the power could be as high as 25% on the largest scales.

Because the error term, $\Delta(r)$, depends only on the magnitude of the vector $\mathbf{r}$ for the effects considered above, it is an even function of $\mathbf{r}$, and thus does not effect the odd imaginary part of the Fourier coefficients of the density field. However, if one were to use only the odd components, one would be in effect throwing out half of one's data, giving an unacceptably large variance in the inferred power spectrum. In any case, these sources of systematic error should be kept in mind when drawing conclusions about the presence of excess power on large spatial scales.

The fact that we are working in redshift space rather than real space introduces another source of distortion to the power spectrum. The linear flow field enhances the apparent clustering in redshift

space, which causes the derived power to increase by a constant factor on large scales (Kaiser 1987). We will measure and calibrate this effect using linear theory and N-body simulations in § 3.3 below.

2.3 Sensitivity of $\tilde{P}(k)$ to the Choice of Sample Geometry

According to Equation 2, if there existed a geometry such that the window function vanished identically for the sampled wavenumber, then the scaling of $\delta_{\mathbf{k}}$ would be exactly proportional to n^{-1}, which would solve the first of the three problems addressed above. One might argue that the sphere is the natural geometry for a full-sky redshift survey, and that it maximizes the survey volume for a given distance limit. A spherical region is particularly desirable when performing analyses in which the galaxies are weighted by the inverse of the selection function (cf. Equation 1) since, by radial symmetry, all galaxies at the boundary of the sample will then be given equal statistical weight.

In that case the window function vanishes for values of kR which are zeros of the $j_1(x)$ Bessel function (cf., Equation 11).

Unfortunately, plane waves are not orthogonal modes when integrated over a sphere. If they were, then the distribution in the plane spanned by the real and imaginary parts of $\delta_{\mathbf{k}}$ would be an isotropic bivariate Gaussian; deviations from isotropy indicate strong correlations between the modes, as well as covariance between the real and imaginary components of a given mode. We have examined the distribution of Fourier components in this plane for Poisson-distributed points. In the spherical geometry the distribution is very anisotropic.

The orthogonality of the modes could be maintained by using spherical waves instead of planar waves. We have chosen not to take this route here, both because we wish our results to be readily compared with the usual description of the power spectrum by means of plane waves, and because we have found another effective way of generating orthogonal planar modes. We use a cylinder with length $2R$ and a circular base of radius R which we align with the direction of $\mathbf{k}$. We therefore give up the idea of maintaining a fixed sampling volume, and different galaxies are used to estimate the power for $\mathbf{k}$'s in different directions. The enclosed sphere of radius R is, of course, common to all the sampling volumes. Since we sample $\mathbf{k}$ in 500 random directions, we are, in effect, sampling a larger sphere of radius $\sqrt{2}R$ with a window which is unity up to a radius of R, and then goes abruptly to zero at the outer edge of the volume.

We now choose our wavenumbers by requiring that $kR = n\pi$ with $n = 1, 2, 3, \ldots$. This not only causes $W(\mathbf{k})$ to vanish, but it also maintains the orthogonality of the modes; unlike the spherical geometry mentioned above, the distribution of $\delta_{\mathbf{k}}$ in the complex plane is quite isotropic.

For long wavelengths, we calculate $\tilde{P}(k)$ only at the harmonic frequencies of the cylinder which is aligned along the $\mathbf{k}$ axis for each direction chosen; as stated earlier, 500 directions are averaged together for our final result. In practice, after the first five harmonics, $W(\mathbf{k})$ is so small as to be negligible in Equation 3; thus for $k > 5\pi/R$, we no longer require k to be a multiple of π/R.

In the case of cylindrical geometry, the convolution integral in Equation 9*b* is given by,

$$\tilde{P}(k) = \frac{V}{(2\pi)^3} \int d^3k' \, P(k') W^2(|\mathbf{k} - \mathbf{k}'|R) \tag{14a}$$
$$= \int_{-\infty}^{\infty} dx' \, F(x') \, j_0^2(x' - kR)$$

where

$$F(x) \equiv \frac{2}{\pi} \int_0^{\infty} \frac{dx'}{x'} J_1^2(x') P\left(\frac{\sqrt{x^2 + x'^2}}{R}\right), \tag{14b}$$

and $j_0(x)$ and $J_1(x)$ are the standard spherical and cylindrical Bessel functions, respectively. As stated above, we do not attempt to deconvolve the $\tilde{P}(k)$ derived from the data, but rather convolve all theoretical predictions using Equations 14 in order to compare with the observed spectrum.

3. Testing the Techniques with N-Body Simulations

3.1. Generation of Mock IRAS Catalogs

In order to test the reliability of our method for extracting the power spectrum, we created a series of mock *IRAS* catalogs drawn from N-body simulations of a CDM universe. The simulations are those used by Górski *et al.* (1989), Frenk *et al.* (1990), and Davis, Strauss, & Yahil (1991), and are of a standard biased CDM universe ($h = 0.5, \Omega = 1, \Lambda = 0,\ n = 1$) computed using a P^3M algorithm with 64^3 particles in a cube of comoving length 180 h^{-1}Mpc. The initial power spectrum in the simulations is that of Davis *et al.* (1985). The simulations are biased in the sense that their output times are chosen to make the *rms* mass fluctuations in an 8 h^{-1}Mpc sphere equal $1/b$; the results presented here use a model with $b = 1.6$. The points selected as *IRAS* galaxies, however, are not biased; they do trace the mass.

The details of how we construct a mock *IRAS* catalog are described in Górski *et al.* (1989) and in Davis *et al.* (1991). Dissipationless N-body models with $\Omega = 1$ tend to be too "hot" on small scales and have velocity dispersions in excess of those observed (e.g., Davis *et al.* 1985). Thus we convolve the velocity field with a Gaussian window of $\sigma = 1$ h^{-1}Mpc in order to reduce the pair dispersion to values close to those observed. We then select those particles in the simulation whose properties match closely those of the Local Group (LG). To be chosen as a LG candidate, the particle must 1) have a peculiar

velocity of $\mathbf{v_p} = 600 \pm 10$ km s^{-1}, 2) reside in a region in which the fractional overdensity, δ, averaged in a radius of 450 km s^{-1} is in the range $-0.2 < \delta < 1.0$, and 3) reside in a region of low shear such that $|\mathbf{v_p} - \langle \mathbf{v} \rangle| < 0.3\mathbf{v_p}$, again within a sphere of radius 450 km s^{-1}. There are 1101 particles in our simulation which satisfy these criteria.

After choosing a suitable LG candidate, we mimic the geometry of the *IRAS* sample by rotating the coordinate system of the N-body model so that the velocity vector of the candidate particle is aligned with the direction of the observed Local Group motion (277°, 30°) as inferred from the dipole moment of the Cosmic Microwave Background (Smoot *et al.* 1991). We construct a flux-limited catalog around a LG candidate by including particles with a probability given by the value of the *IRAS* selection function (cf., § 4.1 below) at the distance between it and the LG. Fluxes are assigned to the remaining objects so that their luminosities are consistent with the *IRAS* luminosity function (as inferred from the derivative of the selection function). The redshift of each particle in the LG rest frame is calculated from its distance, its peculiar velocity, and the peculiar velocity of the LG. The selection function and mean density are then recomputed directly from the redshifts (not distances, in order to mimic what is done with the true *IRAS* sample) of these data for particles within 10,000 km s^{-1} of the LG using the methods of Yahil *et al.* (1991). Finally, particles lying in the regions of the sky not covered by our sample (cf., Strauss *et al.* 1990) are rejected, and these "excluded zones" are filled in with artificial galaxies in exactly the way the real data are treated (Yahil *et al.* 1991; cf., § 4.1 below). We created ten such mock *IRAS* samples centered on ten distinct LG candidates.

3.2. Monte-Carlo Results

Figure 1 shows the mean of the resulting power spectrum, $\tilde{P}(k)$, from our ten mock *IRAS* catalogs for six different sample volumes which correspond to right circular cylinders of length and base diameter 30, 60, 90, 113, 143, and 180 h^{-1}Mpc. The solid symbols in each panel refer to the power spectrum when the real distances to the galaxies are used, while the open symbols refer to the power spectrum computed from the "Local Group" redshifts. In each case, the selection function is calculated self-consistently from the data. The error bars shown are the standard deviations in the estimates of the power from the ten different catalogs at each wavenumber. The dashed horizontal line in each graph is the level of the shot noise term given by Equation 10.

Not surprisingly, as the volume increases, the shot noise contribution rises dramatically. Consequently, for high frequency modes it is desirable to compute the power spectrum in as small a volume as possible. For low frequencies, we must increase the size of the sample to ensure that multiple

wavelengths fit inside the volume; unfortunately, this must be done at the expense of increasing the shot noise contribution to the power. Thus more weight should be given to high frequency modes computed in smaller volumes, where the shot noise contribution is smaller. This behavior can seen in Figure 1 where the errors at high frequency become smaller as the sample volume is decreased from the 180 h^{-1}Mpc to the 60 h^{-1}Mpc cylinder. The volume can not be made arbitrarily small, however, because the variance in the derived power will then be dominated by sampling fluctuations. This is apparent in Figure 1 for the 30 h^{-1}Mpc cylinder. In this case, the errors at high frequency are larger than for the 60 h^{-1}Mpc cylinder, because there are large variations in the local density fields of the CDM realizations.

Figure 2 shows the power spectra from the different volumes plotted on a single graph. The $\tilde{P}(\boldsymbol{k})$ from the different volumes are remarkably consistent despite the fact that the power spectra in different volumes are convolved with different window functions (i.e., different values of R in Equation 14). The mutual consistency of the power spectra suggests that a meaningful way to reduce the high frequency noise in the estimate of $\tilde{P}(\boldsymbol{k})$ is to average the power spectra from the different volumes. Thus our final estimate of the power spectrum is a variance weighted average of the mean power in the different volumes. The error bar for this final estimate is taken to be the minimum of the standard deviations from the different sample volumes. Although this error estimate is not rigorous, it does give a rough idea of the uncertainty in the power. We use this averaging procedure and the corresponding errors merely as a convenient way of presenting the data from the different volumes as a single power spectrum. We stress that the probability distribution for the power is non-Gaussian and the variance is at best only illustrative of the spread of the power at a given frequency. In § 7 below, we use N-body simulations to derive the probability distribution directly, in order to compare the standard CDM model with observed power spectrum; no quantitative analysis is based on the averaged $\tilde{P}(\boldsymbol{k})$ presented here.

Figure 3*a* shows the averaged power spectra in our mock catalogs as measured in real space (i.e., without redshift distortions). The solid curve is the power spectrum as measured from an FFT of the entire simulation, i.e., the "true" power spectrum, convolved with the cylindrical window function given in Equation 14. Although the power spectrum in Figure 3 is an averaged $\tilde{P}(\boldsymbol{k})$ derived from the $\tilde{P}(\boldsymbol{k})$ in different sized volumes, the convolution is performed for a cylinder size of $2R = 180\ h^{-1}$Mpc to ensure that the distortion due to window function is correctly estimated on the largest scales. The power spectrum has been computed at frequencies covering the full dynamic range of the simulations. The agreement is quite good; Figure 3*a* shows that the technique is in fact successful at recovering the true power spectrum. Note in particular that the filling in of excluded zones has a negligible effect on the derived power spectrum.

3.3. Redshift Space Distortions

The power spectrum in redshift space is expected to be distorted from that computed in real space on both large and small scales. On small scales, the amplitude of the power spectrum is suppressed by non-linear effects, while on large scales it is enhanced by streaming motions (Davis *et al.* 1992); consequently, the power spectrum appears steeper when computed in redshift space than in real space. If the virialized peculiar velocities have a Gaussian distribution characterized by a dispersion, σ_v, then the power spectrum on small scales will be modified by

$$P(k) \rightarrow P(k)\frac{\sqrt{\pi}}{2}\frac{\mathrm{erf}(k\sigma_v/H_0)}{k\sigma_v/H_0}, \tag{15}$$

where H_0 is the Hubble constant (cf., Peacock 1991).

On large scales, where linear theory applies, the azimuthally averaged power spectrum is enhanced by a k-independent factor (Kaiser 1987)

$$P(k) \rightarrow f(\Omega, b)\, P(k) \quad \text{where } f(\Omega, b) \equiv \left[1 + \frac{2}{3}\left(\frac{\Omega^{0.6}}{b}\right) + \frac{1}{5}\left(\frac{\Omega^{0.6}}{b}\right)^2\right] \quad . \tag{16}$$

The velocity dispersion in our N-body models is dominated by tight binary pairs with high relative velocity. In order to reduce the velocity dispersion to a level consistent with observations, we smooth the N-body model velocity fields on small scales as mentioned in § 3.1. Due to this smoothing, the suppression of the power spectrum at high frequencies described by Equation 15 will be limited. There will, however, be an enhancement of the power on large scales in accordance with Equation 16. In Equation 16, the appropriate bias is $b = 1$ since the galaxies in our simulations trace the mass; thus on large scales the power spectrum in redshift space is amplified in our simulations by a factor of 28/15.

In Figure 3*b* we plot the mean redshift space power spectrum from the mock *IRAS* catalogs. The solid curve in Figure 3*b* is the real space power spectrum (shown in 3*a*) modified by the large scale distortion in Equation 16. There is good agreement between our measured power spectrum and the expected redshift power spectrum on large scales where Equation 16 is valid. The points in Figure 3*c* show the ratio of the redshift and real space power spectra as a function of frequency. The redshift distortion can be parameterized roughly by the following expression

$$g(k) = \frac{(k/k_c)^n + f(\Omega, b)}{(k/k_c)^n + 1} \quad , \tag{17}$$

with $n = 2$ and $k_c = 2\pi/(20\ h^{-1}\mathrm{Mpc})$. This is shown as the solid curve in Figure 3*c*.

4. Application to the 1.2 Jy Survey

4.1. Sample Selection

The redshift sample used in the analysis of this paper consists of galaxy candidates chosen from the *IRAS* database using a color criterion described in Strauss *et al.* (1990). The sample is complete to a flux limit of 1.2 Jy at 60 μm and contains 5304 galaxies. Forty three objects (0.8% of the total sample) do not have redshifts at this writing. Sky coverage is 96% complete for $|b| > 5°$; our sample thus covers 87.6% of the sky. A further description of the sample and its selection criteria can be found in Strauss *et al.* (1990) and Fisher (1992).

All heliocentric redshifts have been converted to the Local Group reference frame using the transformation given by Yahil, Tammann, & Sandage (1977); "redshift" will refer to redshifts with respect to the Local Group rest frame. We will compute the power spectrum in redshift space, thus no corrections will be made for peculiar velocities. The selection function is computed using the maximum likelihood estimator of Yahil *et al.* (1991) which is unbiased in the presence of density inhomogeneities, using all galaxies with redshift less than 10,000 km s^{-1}. Yahil *et al.* show that the selection function derived to 10,000 km s^{-1} correctly describes the luminosity distribution of galaxies at higher redshifts; thus our derived selection function is valid out to the largest scales for which it is used. We "semi-volume limit" our sample by excluding all objects whose observed flux would fall below 1.2 Jy if they were to be placed at r_s = 635 km s^{-1}; thus we normalize the selection function so that $\phi(r) = 1$ for $r < r_s$. The mean density n is the optimal J_3-weighted sum of all the galaxies within 10,000 km s^{-1} (cf., Davis & Huchra 1982). As discussed in §2.2, the neglect of relativistic and evolutionary effects should not introduce a significant error in our analysis; consequently, we make no correction for these effects.

Our choice of cylindrical sample geometry (outlined in §3.2) requires a sample with full-sky coverage. As in Yahil *et al.* (1991), the region at $|b| < 5°$ is filled with artificial galaxies with a density interpolated from the galaxy distribution at higher latitudes, while the high-latitude excluded zones are filled with the mean density of the survey. In total, 696 random galaxies are added in the excluded zones. We have confirmed using the N-body models described in §3.1 that this interpolation has a negligible affect on our results.

4.2. The 1.2 Jy IRAS Power Spectrum

In Figure 4, we show the *IRAS* power spectrum computed in six different volumes. Error bars represent corresponding variances found in the mock *IRAS* catlogs. We have used the Monte-Carlo

variances in each volume to form a variance-weighted mean spectrum, in the same way as described for the N-body models in §3.2. The mean *IRAS* power spectrum is shown as the solid symbols in Figure 5*a*. This is the central result of this paper.

By using a cross-correlation technique between the QDOT redshift survey and its parent two dimensional catalog, Saunders *et al.* 1992 have inferred that the *real* space correlation function of *IRAS* galaxies on small and intermediate scales ($\lesssim 30\ h^{-1}$Mpc) is given by $\xi(r) = (r/3.79h^{-1}\mathrm{Mpc})^{-1.57}$. This implies that the *IRAS* power spectrum in real space should be $\propto k^{-1.4}$ at high frequencies. However, as discussed in §3.3, the power spectrum will have a somewhat steeper slope when measured in redshift space. In Figure 5*a* the solid line is a power law spectrum $\propto k^{-1.4}$ convolved with the cylindrical window function with $2R = 180\ h^{-1}$Mpc to account for the distortion of $P(k)$ due to the finite volume on large scales. As expected, our *IRAS* power is slightly steeper than this model. The non-linear distortion term given in Equation 15 will yield a steeper power spectrum. Measurements of the correlation anisotropies in the 1.2 Jy *IRAS* catalog suggest that *IRAS* galaxies have $\sigma_v \approx 200$ km s^{-1} (Davis *et al.* 1992). The dashed line in Figure 5*a* is the $k^{-1.4}$ spectrum modified by the redshift distortion factor given in Equation 15 with $\sigma_v = 200$ km s^{-1}. This model appears to be in quite good agreement the observed spectrum for wavelengths $\lesssim 100\ h^{-1}$Mpc. On scales larger than $\sim 100\ h^{-1}$Mpc, the *IRAS* power spectrum begins to deviate from the simple power law model.

We can avoid the subtleties of the redshift distortions by comparing the *IRAS* $\tilde{P}(k)$ with the two-point correlation function in *redshift* space, $\xi(s)$, of the 1.2 Jy survey. In Figure 5*b*, the solid curve is the Fourier transform of the average *IRAS* $\tilde{P}(k)$ shown in Figure 5*a*. The triangles show $\xi(s)$ determined directly from pair counts of the 1.2 Jy survey (Fisher 1992). The power spectrum and correlation function are in excellent agreement.

5. Consistency with Other Determinations

In Figure 6, we compare our power spectrum with a variety of published results. In the first panel, we compare our *IRAS* $\tilde{P}(k)$ with the power spectrum of Peacock (1991) which provided a good empirical fit to the APM angular correlation function. The two solid curves span the range of fits given by Peacock. We have normalized the amplitude of his $P(k)$ to the *rms IRAS* galaxy counts in spheres of radius 8 h^{-1}Mpc in redshift space ($\sigma_8 = 0.8$; Fisher 1992) to account for the weaker clustering strength of *IRAS* galaxies relative to the optically selected galaxies of the APM survey. In addition we have convolved Peacock's power spectrum with the cylindrical window function in Equation 14 for a sample

of length $2R = 180\ h^{-1}$Mpc in an effort to model the distortion of our *IRAS* $P(k)$ on large scales. The agreement is quite good for low wavenumbers, while the discrepancy in slope on small scales simply reflects the redshift space effects in the *IRAS* sample versus the real space power spectrum of the optical sample, derived from angular correlations. Moreover, we confirm the break from a power law in $P(k)$ at $\log k \sim -1.3$, or scales of 200 h^{-1}Mpc.

In panel *b* of Figure 6 we compare the *IRAS* $\tilde{P}(k)$ with the empirical fit to the power spectrum of galaxies from the Center for Astrophysics (CfA) Redshift Survey given in Vogeley *et al.* (1992). Again, to account for the differing clustering strengths of infrared and optical galaxies, we renormalized the CfA result to the *rms IRAS* galaxy counts ($\sigma_8 = 0.8$) and to model the distortions of the *IRAS* $P(k)$ on large scales we convolve their result with our cylindrical window function with $2R = 180\ h^{-1}$Mpc. The agreement is striking. The two power spectra are virtually indistinguishable over the entire range of scales probed. In particular, we confirm the flattening of the power spectrum noticed by Vogeley *et al.* for $\lambda \gtrsim 125\ h^{-1}$Mpc. We do not, however, see any evidence for a turnover in the spectrum.

In panel *c* of Figure 6, we show the predicted variance in cubical cells, $\sigma^2(l)$, from the *IRAS* $\tilde{P}(k)$. The variance in a cubical cell is given by a straightforward integral over the power spectrum (cf., Efstathiou *et al.* 1990*b*). We have used an approximation to this integral given by Peacock (1991),

$$\sigma^2(l) \approx \frac{2}{\pi^2} k_{eff}^3(l)\, P(k_{eff}(l)) \qquad , \tag{18a}$$

where the effective wavenumber, k_{eff}, for a cubical cell of length l is

$$k_{eff} = \frac{\sqrt{12}}{l} \left[\frac{1}{2} \left(\frac{n+1}{2} \right)! \right]^{\frac{1}{n+3}} \qquad . \tag{18b}$$

In Equation 18*b*, n refers to the spectral index characterizing the power spectrum on scales $\lambda \sim 2l$; we use the values of k_{eff} given by Peacock for a spectral index consistent with the APM angular correlation function. The solid curve shows the variance predicted by the 1.2 Jy *IRAS* power spectrum. The dashed lines represent the variance when the power spectrum is perturbed up and down by the standard deviations of the power found in the N-body simulations. The stars show the variances computed directly from the 1.2 Jy survey in spheres and approximately translated to boxes (Bouchet *et al.* 1992) while the triangles are the variances determined by the QDOT redshift survey (Efstathiou *et al.* 1990*b*). The error bars on the QDOT results are the stated 95% confidence limits.

The agreement between the variance inferred from $\tilde{P}(k)$ and the actual variances in the 1.2 Jy sample is quite good. The predicted variances are consistent with the QDOT determinations for the

smallest and largest cells. The QDOT estimate of the variance in the 40 h^{-1}Mpc cell appears to be significantly in excess of both the inferred variance from the power spectra and the variance determined directly from the 1.2 Jy sample. It has been suggested, however, that the QDOT estimate of the variance at 40 h^{-1}Mpc could be a statistical fluke (Park 1991).

6. Qualitative Comparison with Theoretical Models

One of the main difficulties in comparing models with the data is in the normalization of the model power spectra. The standard method of normalizing to the galaxy counts in an 8 h^{-1}Mpc sphere is dubious since the linear models do not model the non-linear evolution. Moreover, the scales contributing to the σ_8 normalization will be affected differentially by the redshift distortions discussed in §3.3. Modes in the fully linear regime will be significantly enhanced relative to their value in real space while non-linear modes will be suppressed.

In this section we content ourselves with a brief visual comparison of the *IRAS* power spectrum with the linear theory predictions of various theoretical models of structure formation; we reserve a quantitative comparison with the standard CDM model for §7. Consequently, we are concerned primarily with the shape of the power spectra and not the exact normalization. Therefore in this section we have chosen to normalize all theoretical predictions to the observed *rms* fluctuations of *IRAS* galaxies when measured in redshift space in a sphere of radius 8 h^{-1}Mpc; for the 1.2 Jy *IRAS* survey this implies a normalization of $\sigma_8 = 0.8$ (Fisher 1992).

The normalized model power spectra are convolved with the cylindrical window function as given in Equation 14 with $2R = 180$ h^{-1}Mpc, to model the distortion of the power spectrum on large scales due to our sample geometry. In addition, since the comparisons are made with linear theory predictions, we restrict the comparison to wavelengths > 20 h^{-1}Mpc. We emphasize that the error bars shown for the *IRAS* power spectrum are not rigorously defined and that the distribution function characterizing the power at a given frequency is non-Gaussian; the reader should not attempt to quantitatively judge the validity of the models described below with a "χ-by-eye" fit.

6.1. Adiabatic Cold Dark Matter Models

The linear theory CDM power spectrum is given by

$$P(k) = \frac{Ak}{\left[1 + \alpha k + \beta k^{3/2} + \gamma k^2\right]^2} \quad , \tag{19}$$

with $\alpha = 1.71l, \beta = 9.0l^{3/2}, \gamma = 1.0l^2$, and $l = (\Omega h^2)^{-1}$ (Davis *et al.* 1985). Standard CDM has the values $h = 0.5$ and $\Omega = 1$. The standard linear theory CDM power spectrum is shown by the solid line in Figure 7. The *IRAS* power spectrum from Figure 5 is shown as the points with error bars. When normalized to the galaxy counts, the standard CDM power spectrum appears to underestimate the observed power on scales $\gtrsim 50\ h^{-1}$Mpc. Again, the error bars in Figure 7 are merely suggestive, and cannot be used to reject standard CDM using χ^2 statistics. In § 7 below, we will use N-body models to calculate the distribution function of the errors in order to calculate the likelihood that the data are consistent with standard CDM.

The amount of power on large scales in the CDM model is controlled by the horizon length at the epoch of radiation and matter equality. Since the horizon length scales as $(\Omega h^2)^{-1}$, the degree of large scale power in the CDM model may be increased by decreasing either the value of the Hubble constant or the value of the cosmological density parameter. Current observations suggest that $h \gtrsim 0.4$, so, lowering the Hubble constant may not be the best solution to increasing the amount of large scale power.

Another way to improve the agreement of CDM with the observations is to introduce a non-zero cosmological constant in such a way that the universe remains flat but $\Omega < 1$. In fact, a model with $\Omega h = 0.2$ and $\Omega_\Lambda = 0.8$ appears to nicely fit the angular correlation function from the APM galaxy survey (Efstathiou *et al.* 1990*a*). The dotted line in Figure 7 is the prediction of a CDM model with $\Omega = 0.2$, $h = 1.0$, and $\Omega_\Lambda = 0.8$. Peacock & Nicholson (1991) also found this model to be a good fit to the power spectrum of radio galaxies. Baumgart & Fry (1991) concluded that a low Ω CDM model (in their case $\Omega h = 0.34$) was the best fit to the power spectrum of optical galaxies as determined from the Center for Astrophysics (Huchra *et al.* 1983) and Pisces-Perseus (Haynes & Giovanelli 1988) redshift surveys, and Park (1991) used this model to fit the density distribution of the *IRAS* redshift survey of Saunders *et al.* (1991). This model appears to provide an excellent fit to the *IRAS* power spectrum.

6.2. Isocurvature Models

We consider here the power spectra for two models based on isocurvature perturbations: CDM with isocurvature fluctuations, and a baryon-dominated universe with isocurvature fluctuations. The power spectrum for scale invariant isocurvature CDM perturbations is given by

$$P(k) = \frac{Ak}{\left[1 + \left(\alpha k + (\beta k)^{3/2} + (\gamma k)^2\right)^\nu\right]^{1/\nu}}, \tag{20}$$

with $\alpha = 15.6l$, $\beta = 0.9l$, $\gamma = 5.8l$, $\nu = 1.24$, and $l = (\Omega h^2)^{-1}$ (Efstathiou 1991). The short-dashed curve in Figure 7 shows the isocurvature spectrum for $h = 0.5$ and $\Omega = 1$. Although the fit to the *IRAS*

spectrum is quite good, this model is already ruled out by measurements of anisotropies in the microwave background (Efstathiou & Bond 1986).

The second isocurvature model we examined is the baryon isocurvature model of Peebles (1987). This model was designed with the intention of providing more power on large scales than does CDM. The long-dashed curve in Figure 7 shows the spectrum from a fully ionized model with $\Omega = 0.2$, $h = 0.5$, and $n = -1$; we are grateful to Nicola Vittorio for providing this spectrum. The model predicts excessive fluctuations on large scales which appear inconsistent with the data.

6.3. String and Texture Models

The dot-dashed curve in Figure 7 shows the predicted power spectrum from a cosmic string network evolving in a flat universe dominated by Cold Dark Matter. The power spectrum shown is taken from Albrecht & Stebbins (1991) and is given by

$$P(k) = \frac{Ak}{[1 + (\alpha_2 k) + (\alpha_3 k)^2 + (\alpha_4 k)^3]} \left(\frac{1}{1 + (\alpha_5 k)^2} \right)^2 , \tag{21}$$

with $\alpha_2 = 7.57l$, $\alpha_3 = 5.89l$, $\alpha_4 = 1.93l$, $\alpha_5 = 0.000357l$, and $l = h^{-2}$ ($h = 1$ in Figure 7). This power spectrum is based on the numerical simulations of Bennett & Bouchet (1990) and Allen & Shellard (1990), and assumes that the string network is characterized by a scaling solution and that the power is dominated by the coherent motions of long strings; perturbations induced by string loops are neglected in their analysis. As noted by Albrecht and Stebbins, the string power spectrum is much shallower than the other spectra we have considered so far; when it is normalized to the galaxy counts it has a deficit of power on large scales. Comparison of the string spectrum to the *IRAS* power spectrum shows that this is indeed the case. The string spectrum does a very poor job of reproducing the observed power spectrum.

Recently there has been considerable interest in the formation of structure within a CDM universe with perturbations seeded by textures (cf., Gooding, Spergel, & Turok 1991; Cen *et al.* 1991). The long dash-dotted curve in Figure 7 shows the CDM-texture power spectrum from Turok (1991) as quoted in Peacock (1991),

$$P(k) = \frac{Ak}{\left[1 + \left(\alpha k + (\beta k)^{3/2} + (\gamma k)^2\right)^{\nu}\right]^{1/\nu}} , \tag{22}$$

with $\nu = 1.2$, $\alpha = 19.4l$, $\beta = 6.6l$, $\gamma = 3.0l$, and $l = (\Omega h^2)^{-1}$. In Figure 7 we show this spectrum for the case $h = 0.5$ and $\Omega = 1$. Peacock (1991) noted that this spectrum gave an excellent fit to the power spectrum of his radio galaxy survey (Peacock & Nicholson 1991) as well as the CfA results from Baumgart & Fry (1991) and the variance in cells from the QDOT *IRAS* survey (Efstathiou *et al.* 1990*b*). We too

find that the CDM + texture model provides a very good fit to the data. Although the non-Gaussian nature of the string and texture models means that the power spectrum does not provide a full description of the density field even in the linear regime, the power spectrum is still a well-defined quantity, and it is meaningful to compare it to observations.

7. Quantitative Comparison with Standard CDM

The N-body tests described in §3 were adequate for checking the overall effectiveness of our technique for measuring the power spectrum. To access the validity of a cosmological model, however, ten observers from a *single* N-body realization are not sufficient to map out the probability distribution of power at a given frequency. In order to ascertain the goodness of fit between a model and the data, one requires a large number of catalogs constructed from *independent* realizations of the density field of the model. Multiple catalogs drawn from a single realization will probe the distribution of power due to dilute sampling fluctuations, but only independent realizations will properly account for statistical fluctuations in the underlying power spectrum.

Unfortunately, it is computationally impractical for us to evolve a sufficient number of large scale N-body realizations of a CDM universe using methods with enough force resolution to accurately model highly non-linear evolution on small scales (using e.g., PM or P^3M techniques). However, since we are primarily interested in measuring the power spectrum on large scales, we can accurately model the large scale evolution of a CDM universe using the Zel'dovich approximation (Zel'dovich 1970). We use the methods of Efstathiou *et al.* (1985) to generate positions and velocities consistent with the growing mode solution for different realizations of the $\Omega = 1$, $h = 0.5$ CDM power spectrum given in Equation 19. Our simulation volume is a cube of size 180 h^{-1}Mpc, which corresponds to the largest volume in which we measured the *IRAS* power spectrum, namely cylinders of length and diameter 180 h^{-1}Mpc. Like our full N-body runs described in §3, the simulations are unbiased (light traces mass) with 64^3 particles, while the potential is computed on a 128^3 mesh.

For each realization a single mock *IRAS* catalog is extracted using the procedure outlined in §4.1. The analysis of this section is based on 100 such catalogs. For each catalog, we compute the power spectrum in an identical manner as for the *IRAS* sample; in particular, the calculation is done in redshift space. The *IRAS* excluded zones are deleted and interpolated using the procedure of §4.1. In addition, the selection function is self-consistently computed for each catalog. We have computed the power in each of the 100 realizations at frequencies corresponding to the first five harmonics of the 180 h^{-1}Mpc

cylinder, i.e., at $2\pi/k = 180$, 90, 60, 45, and 36 h^{-1}Mpc. The 100 realizations are sufficient to accurately map out the probability distribution of the power at a given frequency.

In order to compare the outcome of the simulations with the *IRAS* $\tilde{P}(k)$, we need to normalize the amplitude of the simulated CDM power spectra. Unfortunately, the Zel'dovich algorithm does not model the non-linear evolution accurately enough to allow the amplitude of the simulations to be matched to the non-linear portion of the *IRAS* power spectrum. We therefore adopt the following procedure to normalize the CDM simulations. We first note that the *real* space *IRAS* correlation function is given by $\xi(r) = (r/3.79h^{-1}\mathrm{Mpc})^{1.57}$ (Saunders *et al.* 1992). This implies that the variance of *IRAS* galaxy counts in *real* space in a sphere of radius 8 h^{-1}Mpc is given by $\sigma_8 = 0.7$. (Recall that in redshift space $\sigma_8 = 0.8$; the two estimates differ due to the redshift distortions discussed in §3.3.) By normalizing the full non-linear power spectrum of our P^3M simulations (determined from an FFT of all 64^3 particles in real space) to $\sigma_8 = 0.70$ we can determine the correct amplitude of real space power spectra in our Zel'dovich models, by matching them to the P^3M simulations at large scales. Next we adopt a bias (which can be varied) and multiply the real space power spectrum by the redshift distortion factor, $f(\Omega, b)$ given in Equation 16; this gives the correct amplitude of the power spectrum in redshift space on large scales. Thus, for a given choice of bias we can renormalize our 100 realizations to give the correct mean value of the power in redshift space on large scales.

To compare with the *IRAS* $\tilde{P}(k)$, we convolve this power spectrum with the window function in Equation 14 for a cylinder of length 180 h^{-1}Mpc. With this normalization, we can directly compare the power in our 100 realizations with the *IRAS* $\tilde{P}(k)$ determined in the same volume (cf., Figure 4*a*). Moreover, we can determine the consistency of the CDM model with the data as a function of the bias factor. The bias factor b used here relates the *IRAS* and dark matter distributions. On small scales the *IRAS* galaxies show somewhat weaker clustering than do optical galaxies (Lahav, Nemiroff, & Piran 1990; Strauss *et al.* 1992a; Fisher 1992), while on large scales the distribution of the two are consistent (Strauss *et al.* 1992a). Thus it is not straightforward to relate the bias factors discussed here directly to that relevant for optical galaxies.

Figure 8 shows an example of the power distribution in our 100 catalogs in the form of a histogram for the first five harmonics of the 180 h^{-1}Mpc cylinder. The model in Figure 8 was normalized with a bias value of $b = 1.0$. The vertical dashed lines in Figure 8 show the observed values of the *IRAS* $\tilde{P}(k)$ at the corresponding frequency, while the percentages listed are the fraction of the simulations having power equal to or in excess of the *IRAS* value. The mean and variances, as well as the two-sided confidence intervals about the median for the data in Figure 8, are given in Table 1. Also listed in Table

1 are the 95% confidence intervals for the power measured by 100 observers drawn from a single N-body realization; note that the power range is a factor of 1.4 smaller at the lowest frequency, demonstrating that dilute sampling is not the limiting error here. The very large spread in the distribution of power on the largest scales is entirely a result of the limited volume of the survey, whereas for the fourth and fifth harmonic, the dilute sampling noise appears to be the limiting factor.

In the limit that the power distribution at a given frequency is dominated by the intrinsic variations in the density field, the probability of measuring a value of the power between p and $p + dp$, at a wavenumber k characterized by a mean power $P(k)$, follows a χ^2 distribution with ν degrees of freedom in the variable $2p\nu/P(k)$. The number of degrees of freedom, ν, is given by the number of ***independent*** Fourier modes at that frequency. Explicitly,

$$f(p) = \frac{\nu^\nu}{\Gamma(\nu)} \left(\frac{p}{P(k)}\right)^\nu \frac{\exp(-\nu p/P(k))}{p} \quad . \tag{23}$$

This is simply because the power is the average of the square of the real and imaginary Fourier coefficients of the density field which themselves are normally distributed with mean zero. Unfortunately, unless we are dealing with a periodic cubical sample (for which the window function in k-space is a delta function), it is difficult to count the number of independent Fourier modes. One does expect a rough scaling, however, $\nu \propto k(k+1)$ for the kth harmonic in the box.

If one makes the ansatz that Equation 23 is correct, then ν is simply related to the moments of the power distribution by $\nu_{eff} = 2P^2/\sigma^2$ where σ^2 is the variance of the distribution. The effective number of degrees of freedom computed in this way are listed in Table 1, and the resulting distribution functions are drawn as the solid curves in Figure 8. Equation 23 no longer adequately describes the power distribution when dilute sampling fluctuations are important. In this case the shot noise couples to the higher moments of the distribution in a complicated way that depends on the sample geometry. Note that the expected scaling for ν_{eff} works reasonably well for the first three harmonics, but fails for the higher harmonics where ν_{eff} is less than predicted (i.e., the distribution is wider than predicted by the scaling law). This is the domain where dilute sampling noise begins to dominate in this large box, and it is consistent with the similarity of the 95% confidence intervals listed in Table 1 for the power computed from 100 observers in a single realization with that for 100 observers in different realizations.

For a given choice of bias, we would like to obtain an overall likelihood that the standard CDM model is consistent with the *IRAS* data. At each of the five frequencies considered, we can determine the fraction of the N-body catalogs with power equal to or in excess of the the observed *IRAS* $\tilde{P}(k)$ at the

corresponding frequency. In order to quote an overall probability that the CDM model can produce power on large scales consistent with the *IRAS* data, one needs to know the covariance between the different frequencies. The cylindrical shape of the analysis volume leads one to expect little covariance between the different harmonics, because the modes are all orthogonal to each other, as we argued in § 2.3. We have checked this empirically by examining the scatter diagrams of the measured power $(\tilde{P}(k_i), \tilde{P}(k_j))$ in the five different harmonics of the 100 realizations. Absolutely no covariance is detected; each plot was consistent with complete scatter. Thus the joint probability density P_T for measuring power with an amplitude consistent with the *IRAS* power at all five frequencies in a CDM universe with a given value of b is simply the product of the fractions at each frequency of the N-body observers having power equal to or exceeding the *IRAS* power. The probability of consistency with the CDM model is then given by the probability of observing a product of the five percentages less than the measured value. The individual percentages, $f(k_1)$, $f(k_2)$, etc. lie in the range $\{0, 1\}$. The probability P_c that their product is less the observed value $P_T = f(k_1)f(k_2)\ldots f(k_5)$ is given by the volume in the five dimensional space spanned by $f(k_1)$, $f(k_2)\ldots$, and $f(k_5)$ and bounded by the level surface where their product equals P_T. The resulting distribution is (Feller 1966),

$$P_c = P_T \sum_{n=0}^{4} \frac{(-\ln(P_T))^n}{n!} \quad . \tag{24}$$

In Figure 9, the solid curve is the probability, P_c, that the standard CDM model is consistent with the *IRAS* $\tilde{P}(k)$, as a function of the *IRAS* to dark matter bias factor. The standard CDM model is consistent with the *IRAS* data for low values of b. Values of the bias exceeding 1.5 are ruled out at the 95% confidence level, while values $b > 2$ are ruled out at the 99% confidence level. The dot-dashed line in Figure 9 shows the probability of consistency, P_c, derived from 100 catalogs drawn from a single realization of the CDM power spectrum. In this case the variance is due solely to sampling fluctuations and is consequently underestimated on large scales (Table 1). The inferred limits on the bias from the single realization are $b < 1.2$ (95% C.L.) and $b < 1.5$ (99% C.L.). Thus, using a single realization one would wrongly infer much more stringent constraints on the bias.

We stress that our analysis only considers the quality of the fit between the *IRAS* and CDM power spectra for wavelengths $> 36\ h^{-1}$Mpc; with our Zel'dovich models we are unable to accurately model the small scale behavior of the clustering. The low values of the bias favored on large scales lead to excessive small scale power. This can be seen in Figure 10 which shows the full non-linear $\tilde{P}(k)$ in *real* space for the N-body simulation described in §3; the spectrum has been normalized to the variance of *IRAS* galaxies in real space as inferred from $\xi(r)$ ($\sigma_8 = 0.7$). Also shown in Figure 10 is the *IRAS* $\tilde{P}(k)$, converted

to "real" space by correcting the raw redshift power by the distortion factor given in Equation 17 with $\Omega = 1$ and $b = 1$. This corrected spectrum is then a good approximation to the *IRAS* power spectrum in real space if they are unbiased tracers of the mass distribution. It is apparent from the figure that while the CDM model fits the *IRAS* power spectrum well on large scales if *IRAS* galaxies are unbiased, it produces excessive power on small scales. This problem might simply be a reflection of adopting a linear biasing model. It remains to be seen whether the standard CDM model can be reconciled with large scale observations by invoking a non-linear biasing mechanism (cf., Babul & White 1991; Bower *et al.* 1992).

The recent COBE detection (Smoot *et al.* 1992) of a large scale anisotropy in the microwave background implies that fixing CDM's problems with non-linear biasing will be difficult at best. In Figure 10, the box shows the large scale power spectrum allowed by COBE for a Harrison-Zel'dovich spectrum with $\epsilon_H = (5.4 \pm 1.6)\text{x}10^{-6}$ (Wright *et al.* 1992). When normalized to the *IRAS* variance, the standard CDM model has insufficient amplitude on large scales to be consistent with the COBE measurements. Conversely, the discrepancy with *IRAS* on small scales becomes worse if the normalization of the standard CDM model is forced to match the COBE result.

8. Discussion

We have presented a technique for recovering the power spectrum in flux-limited galaxy catalogs, and have demonstrated with mock *IRAS* catalogs constructed from CDM simulations that the technique works with observational samples of the size considered in this paper. The power spectrum of *IRAS* galaxies is consistent with a power law, $P(k) \propto k^{-1.4}$, for scales $2\pi/k \lesssim 100\ h^{-1}$Mpc, while on larger scales it begins to flatten. Our results are consistent with recent measurements of large scale power from the angular correlation function of faint galaxies (Peacock 1991), and the power spectrum of galaxies in the CfA survey (Vogeley *et al.* 1992). These other studies all use independent data over only partly overlapping volumes of space. The self-consistency of these studies increases the credibility of their most striking conclusion: there is observed to be more power on wavelengths above 100 h^{-1}Mpc than predicted in a standard CDM model normalized to the observed small scale fluctuations. On large scales, the standard adiabatic CDM model predicts a power spectrum which is very flat. By choosing a low value of the bias, the amplitude of the CDM spectrum can be made consistent with the *IRAS* $\tilde{P}(k)$ on *large* scales. From our Monte-Carlo experiments, the value of the *IRAS* to dark matter linear bias must be $b < 1.5$ at the 95% confidence level and $b < 2$ at the 99% confidence level. Yet, when normalized to the amplitude of the *IRAS* power spectrum on large scales, models with such low values of the bias

produce excessive small scale power. Future investigations may show whether this discrepancy can be avoided by invoking a non-linear biasing mechanism.

This discrepancy can be removed by considering CDM models with lower values of Ωh. In particular, we find that a CDM model with $\Omega = 0.2$, $h = 1$, and $\Omega_\Lambda = 0.8$ provides an excellent fit to the data. However, low values of Ω are not consistent with the *IRAS* velocity field comparisons (Strauss *et al.* 1992b; Dekel *et al.* 1992). The isocurvature CDM model provides a good fit to the data but the model violates current upper limits in the microwave background anisotropies. The isocurvature baryon power spectrum is in excess of the data on large scales, while the string model predicts too little power on large scales and too much power on small scales. Finally, the texture model in a CDM universe agrees well with the data and merits further attention. Unlike the low-Ω CDM model considered above, the texture model predicts a non-Gaussian density field even on linear scales; future work will test this aspect of the models against the data (cf., Nusser & Dekel 1992).

Our measured power spectrum is consistent with and complements previous analyses, but we believe the *IRAS* catalog has several important advantages. Our sample probes a larger volume, albeit with sparser sampling, than does the CfA analysis by Vogeley *et al.* (1992), and our survey geometry is full sky, rather than a complex cone in redshift space. Thus our window function is rather simple, and leads to little smearing of the measured power spectrum. This allows us to work with orthogonal plane waves in cylindrical volumes, giving us a direct measure of $\tilde{P}(k)$ with essentially no covariance between modes. This in turn allows a very direct statistical assessment of the likelihood of consistency with any given model. The CfA survey, with its denser sampling, is better suited than our *IRAS* sample for determining $P(k)$ on small wavelengths although the agreement on all scales is excellent.

In spite of our large survey volume, the error in the determination of the large scale power is still too large to convincingly measure an approach to the primordial Zel'dovich spectrum. For standard CDM, this happens on wavelengths of $\sim 150\ h^{-1}$Mpc, and for $\Omega h = 0.2$ CDM, the scale is 2.5 times larger. Such a measurement would require at least a tenfold increase in sample size and survey volume over those currently available. Such projects are currently in the planning stage. If future surveys are to lead to improved measures of the power spectrum on scales of $\gtrsim 200\ h^{-1}$Mpc, it is essential that they be designed with careful attention given to the shape and sampling density.

We have computed the amplitude of small scale fluctuations in the CMB expected in a universe with fluctuations given by our measured power spectrum; these results will be reported in due course (Fisher 1992), and are of direct interest to the current generation of CMB isotropy experiments.

KBF acknowledges the support of a Department of Education Graduate Fellowship. This work has been supported in part by grants from NSF and NASA.

TABLE 1

Confidence Levels for CDM Monte-Carlo Simulations for $b = 1.0$

	CDM $\langle\tilde{P}(k)\rangle/(2\pi)^3\,(\mathrm{h\,Mpc})^3$						IRAS $\langle\tilde{P}(k)\rangle/(2\pi)^3\,(\mathrm{h\,Mpc})^3$	
$2\pi h/k$ Mpc	mean	stn. dev.	ν_{eff}	68% C.L†	95% C.L.††	99% C.L.		$P(p_{IRAS})$†††
180	20.0	13.4	2	6.4-30.1	2.7-54.9 (3.4-39.7)	1.6-61.7	36.1	0.13
90	20.1	7.8	6	12.6-27.7	8.1-42.2 (8.1-33.9)	4.0-44.5	27.9	0.16
60	17.4	5.6	9	11.8-23.4	7.8-29.2 (8.8-27.8)	7.0-35.4	17.1	0.52
45	14.8	3.9	14	10.2-19.0	8.2-20.7 (6.2-25.0)	6.0-28.2	13.6	0.61
36	11.4	3.4	10	8.4-15.2	5.1-19.7 (5.6-18.4)	2.9-20.5	11.1	0.51

† Two-sided confidence intervals.

†† Limits in parentheses are for 100 *IRAS* catalogs drawn from a *single* realization of CDM density field

††† Percentage of models with power equal to or exceeding the *IRAS* power

References

Albrecht, A., & Stebbins, A. 1991, preprint

Allen, B., & Shellard, P. 1990, Phys. Rev. Lett., 64, 119

Babul, A., & White, S.D.M. 1991, MNRAS, 253, 31P

Baumgart, D. J., & Fry, J. N. 1991, ApJ, 375, 25

Bennett, D., & Bouchet, F. 1990, Phys. Rev. D, 40, 973

Bertschinger, E., & Juszkiewicz, R. 1988, ApJ, 334, L59

Bouchet, F. R., Davis, M., & Strauss, M., proceedings of the DAEC workshop, March 91, in press

Bower, R.G., Coles, P., Frenk, C.S., & White, S.D.M. 1992, preprint

Cen, R.Y., Ostriker, J.P., Spergel, D.N., & Turok, N. 1991, ApJ, 383, 1

Davis, M., Efstathiou, G., Frenk, C.S., & White, S.D.M. 1985, ApJ, 292, 371

Davis, M., Fisher, K.B., Strauss, M.A., Yahil, A., & Huchra, J.P. 1992, in preparation

Davis, M., & Huchra, J.P. 1982, ApJ, 254, 437

Davis, M., & Peebles, P.J.E. 1983, ApJ, 267, 465

Davis, M., Strauss, M.A., & Yahil, A. 1991, ApJ, 372, 394

de Lapparent, V., Geller, M.J., & Huchra, J.P. 1988, ApJ, 332, 44

Dekel, A., Bertschinger, E., Yahil, A., Strauss, M.A., Davis, M., & Huchra, J.P. 1992, in preparation

Efstathiou, G. 1991, in Physics of the Early Universe, eds. J.A. Peacock, A.F. Heavens, & A.T. Davies (Edinburgh: SUSSP), p. 361

Efstathiou, G., & Bond, J.R. 1986, MNRAS, 218, 103

Efstathiou, G., Davis, M., Frenk, C.S., & White, S.D.M. 1985, ApJS, 57, 241

Efstathiou, G., Ellis, R.S., & Peterson, B.A. 1988, MNRAS, 232, 431

Efstathiou, G., Sutherland, W. J., & Maddox, S. J., 1990*a*, Nature, 348, 705

Efstathiou, G., Kaiser, N., Saunders, W., Lawrence, A., Rowan-Robinson, M., Ellis, R.S., & Frenk, C.S. 1990*b*, MNRAS, 247, 10

Gramann, M. & Einasto, J. 1991, MNRAS, 254, 453

Feller, W. 1966, An Introduction to Probability Theory and its Applications, Vol. II, (New York: John Wiley & Sons, Inc.)

Fisher, K.B. 1992, PhD. thesis, University of California, Berkeley

Fisher, K.B., Strauss, M.A., Davis, M., Yahil, A., & Huchra, J.P. 1992, ApJ, 389, 188

Frenk, C.S., White, S.D.M, Efstathiou, G., & Davis, M. 1990, ApJ, 351, 10

Gooding, A.K., Spergel, D.N., & Turok, N. 1991, ApJ, 372, L5

Górski, K., Davis, M., Strauss, M.A., White, S.D.M., & Yahil, A. 1989, ApJ, 344, 1

Hamilton, A.J.S., Kumar, P., Lu, E., & Matthews, A. 1991, ApJ, 374, L1

Haynes, M.P., & Giovanelli, R. 1988, in Large-Scale Motions in the Universe, eds. V.C. Rubin & G.V. Coyne, S.J. (Princeton: Princeton University Press), p. 31

Huchra, J., Davis, M., Latham, D., & Tonry, J. 1983, ApJS, 52, 89

Kaiser, N. 1987, MNRAS, 227, 1

Kaiser, N. 1991, preprint

Lahav, O., Nemiroff, R.J., & Piran, T., 1990, ApJ, 350, 119

Maddox, S.J., Efstathiou, G., Sutherland, W., & Loveday, J. 1990, MNRAS, 242, 43P

Nusser, A., & Dekel, A. 1992, preprint

Park, C. 1991, ApJ, 382, L59

Park, C., Gott, R. J., & da Costa, L. N. 1992, ApJL, submitted

Peacock, J. A. 1991, MNRAS, 253, 1P

Peacock, J. A., & Nicholson, D. 1991, MNRAS, 253, 307

Peebles, P. J. E. 1980, The Large-Scale Structure of the Universe, (Princeton: Princeton University Press)

Peebles, P.J.E. 1987, Nature, 327, 210

Saunders, W., Frenk, C.S., Rowan-Robinson, M., Efstathiou, G., Lawrence, A., Kaiser, N., Ellis, R.S., Crawford, J., Xia, X.-Y., & Parry, I. 1991, Nature, 349, 32

Saunders, W., Rowan-Robinson, M., & Lawrence, A. 1992, MNRAS, in press

Saunders, W., Rowan-Robinson, M., Lawrence, A., Efstathiou, G., Kaiser, N., Ellis, R.S., & Frenk, C.S. 1990, MNRAS, 242, 318

Smoot, G.F. *et al.* 1991, ApJ, 371, L1

Smoot, G.F. *et al.* 1992, preprint

Strauss, M.A., Davis, M., Yahil, A., & Huchra, J. P. 1990, ApJ, 361, 49

Strauss, M.A., Davis, M., Yahil, A., & Huchra, J. P. 1992a, ApJ, 385, 421

Strauss, M.A., Yahil, A., Davis, M., Huchra, J.P., & Fisher, K.B. 1992b, ApJ, in press

Turok, N. 1991, in proc. Nobel Symposium # 79, eds. J.S. Nilsson, B. Gustafsson, & B.-S. Skagerstam, Physica Scripta, T36, 135

Vogeley, M.S., Park, C., Geller, M.J., & Huchra, J.P. 1992, ApJL, 395, L5

Wright, N. *et al.* 1992, preprint

Yahil, A., Strauss, M.A., Davis, M., & Huchra, J.P. 1991, ApJ, 372, 380

Yahil, A., Tammann, G.A., & Sandage, A. 1977, ApJ, 217, 903

Zel'dovich, Y.B. 1970, A&A, 5, 84

Figure Captions

Figure 1. The mean power spectrum from the ten mock *IRAS* catalogs constructed from our CDM simulations. The power spectrum is computed in six different volumes corresponding to right circular cylinders of length *a*) 180, *b*) 143, *c*) 113, *d*) 90, *e*) 60, and *f*) 30 h^{-1}Mpc. The solid and open symbols in each panel are the power spectrum computed in real and redshift space respectively. The dotted line in each panel is the shot noise contribution (cf., Equation 10). Errors are the standard deviation of the measurements from the ten mock *IRAS* catalogs.

Figure 2. The power spectra in Figure 1 for all the volumes considered in *a*) real space and *b*) redshift space. Note the consistency between the various volumes despite the effects of the convolution in Equation 14.

Figure 3. Final average estimate of the power spectrum in *a*) real and *b*) redshift space for our mock *IRAS* catalogs. The solid curve in *a*) is the power spectrum obtained from a FFT on the entire simulation in real space. The curve in *b*) is the real space FFT power spectrum modified by the redshift space distortion factor given in Equation 16. *c*) Points are the ratio of the redshift to real space power spectra given in *a* and *b* for the ten mock *IRAS* N-body observers. The upper dashed line corresponds to the linear theory value of 28/15 derived by Kaiser (1987) while the lower dotted line corresponds to unity. The solid curve is the empirical fit described in the text.

Figure 4. Estimate of the *IRAS* power spectrum for six volumes corresponding to right circular cylinders of length *a*) 180, *b*) 143, *c*) 113, *d*) 90, *e*) 60, and *f*) 30 h^{-1}Mpc. Dotted lines in each panel represent the shot noise contribution to the power (cf., Equation 10). Errors are taken from the CDM Monte-Carlo spectrum (cf., Figure 3).

Figure 5. Panel *a*) shows the final variance weighted estimate of *IRAS* power spectrum. The solid curve in *a*) represents the power law power spectrum which is consistent with the real space *IRAS* two-point correlation function ($P(k) \propto k^{-1.4}$) convolved with the cylindrical window function (cf., Equation 14). The dashed curve is the same power law modified by the non-linear redshift distortion factor given in Equation 15 with $\sigma_v = 200$ km s^{-1}. The solid curve in panel *b*) is the Fourier transform of the *IRAS* power spectrum in *a*). The triangles in *b*) are the redshift space two-point correlation function of the 1.2 Jy sample (Fisher 1992).

Figure 6. Comparison of the *IRAS* power spectrum with previous results in the literature. *a*) Solid curves denote $P(k)$ as determined by Peacock (1991), who fit a model spectrum to the APM $w(\theta)$. The two curves span the quoted uncertainties in the fit. Peacock's $P(k)$ has been convolved with the cylindrical window function in Equation 14 and normalized to the observed *IRAS* variance in redshift space, $\sigma_8^2 = 0.64$. *b*) Solid curve is the best fit power spectrum of the CfA sample from Vogeley *et al.* (1992). As in *a*, the CfA $P(k)$ has been convolved with the cylindrical window function and normalized to the observed *IRAS* variance. *c*) Solid line is the predicted *IRAS* counts in cells determined from *IRAS* $\tilde{P}(k)$ using the prescription of Peacock (1991); dashed lines represent the predicted counts when by the *IRAS* $\tilde{P}(k)$ is increased or decreased by the errors determined from the N-body simulations. The stars represent the counts in cells from the 1.2 Jy survey (Bouchet *et al.* 1992), while triangles represent the counts in the QDOT survey (Efstathiou *et al.* 1990). Error bars are the 95% confidence limits.

Figure 7. Comparison of the *IRAS* power spectrum, $\tilde{P}(k)$, with various linear theory models. All models have been convolved with the cylindrical window function in Equation 14 and normalized to the *IRAS* variance (in redshift space) in a sphere of radius 8 h^{-1}Mpc. Frequencies corresponding to $\lambda = 20 - 180$ h^{-1}Mpc are plotted. Power spectra are described in the text.

Figure 8. Power histograms for the Zel'dovich Monte Carlo simulations of standard CDM. The histograms show the distribution of the power computed in 100 mock *IRAS* catalogs for the first five harmonics of the 180 h^{-1}Mpc cylinder normalized to $b = 1.0$. The dashed lines in each panel represent the observed value of the *IRAS* $\tilde{P}(k)$ for the same wavenumber. The solid curves represent the expected χ^2 distribution if the scatter in the power is due strictly to the fluctuations induced by different realizations.

Figure 9. Probability that the standard CDM model can produce power of sufficient amplitude on large scales to be consistent with the *IRAS* $\tilde{P}(k)$ as a function of the adopted linear bias. The solid curve is derived from 100 independent realizations of the CDM power spectrum, while the dot-dashed is the probability derived from 100 catalogs drawn from a single realization of the CDM spectrum.

Figure 10. Solid curve is the power spectrum of the full non-linear CDM N-body simulation (as in Figure 3) normalized to the real space variance of *IRAS* galaxies ($\sigma_8 = 0.7$). The points are the *IRAS* redshift space $\tilde{P}(k)$ from Figure 4, rescaled by Equation 17 with $\Omega = 1$ and $b = 1$; this is then an approximation to the power spectrum of *IRAS* galaxies in *real* space on large scales if the *IRAS* galaxies are unbiased. The box indicates the power spectrum inferred from the COBE DMR measurements, assuming a $n = 1$ spectral index and $\epsilon_H = (5.4 \pm 1.6)\text{x}10^{-6}$ (Smoot *et al.* 1992; Wright *et al.* 1992). The box is drawn over the wavelength range of 3000 h^{-1}Mpc (corresponding to the horizon size) to 1000 h^{-1}Mpc ($\sim 10°$ on the sky). Note that when the CDM model is normalized to the *IRAS* variance, it produces excessive power on small scales while simultaneously failing to produce sufficient power on large scales to match the COBE results.

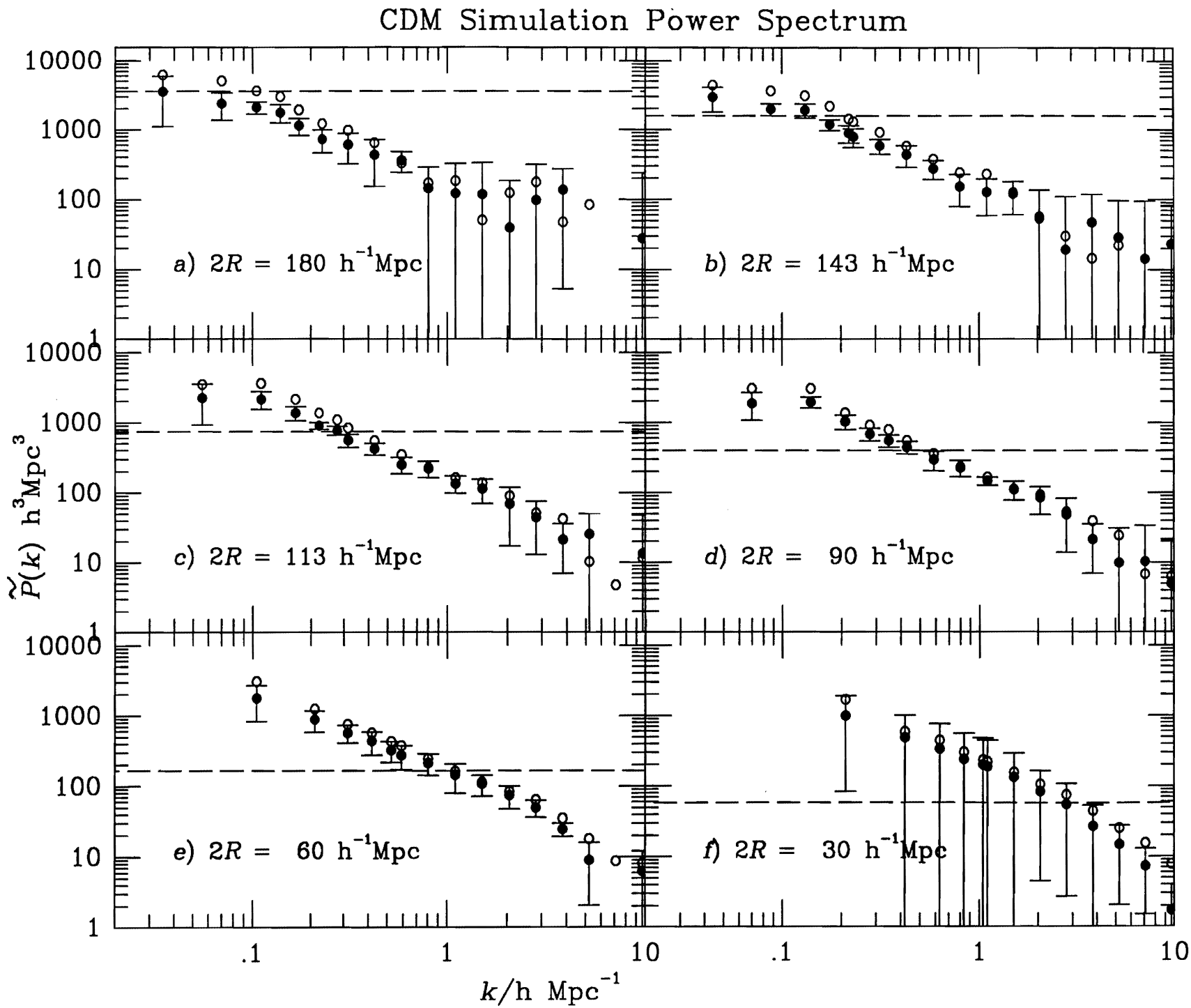
CDM Simulation Power Spectrum
a) 2R = 180 h⁻¹Mpc
b) 2R = 143 h⁻¹Mpc
c) 2R = 113 h⁻¹Mpc
d) 2R = 90 h⁻¹Mpc
e) 2R = 60 h⁻¹Mpc
f) 2R = 30 h⁻¹Mpc
P̃(k) h³Mpc³
k/h Mpc⁻¹
10000
1000
100
10
1
.1
1
10

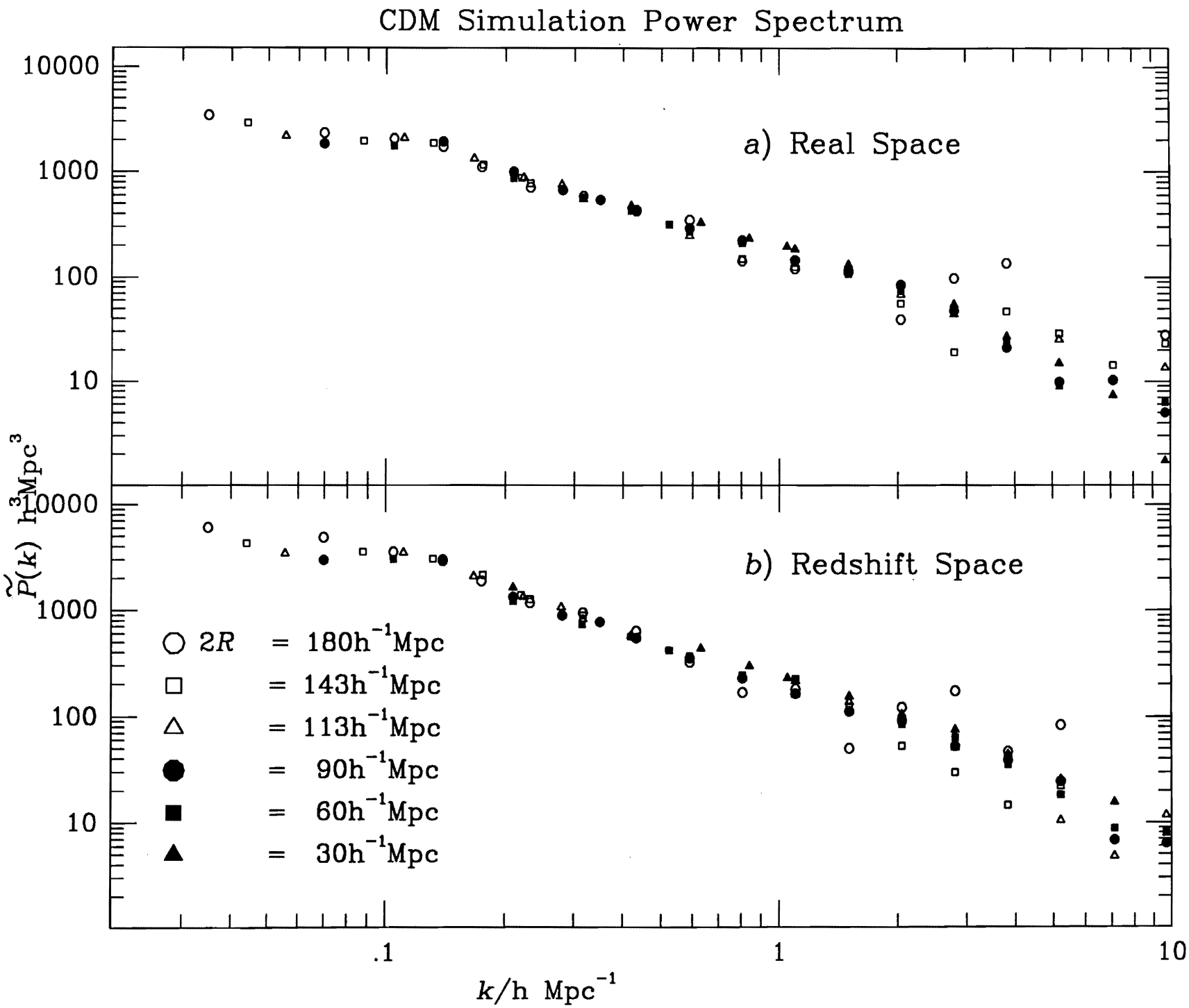
CDM Simulation Power Spectrum
a) Real Space
b) Redshift Space
10000
1000
100
10
.1
1
10
$\tilde{P}(k)$ h^{-3}Mpc^3
k/h Mpc^{-1}
$2R$ = 180h^{-1}Mpc
= 143h^{-1}Mpc
= 113h^{-1}Mpc
= 90h^{-1}Mpc
= 60h^{-1}Mpc
= 30h^{-1}Mpc

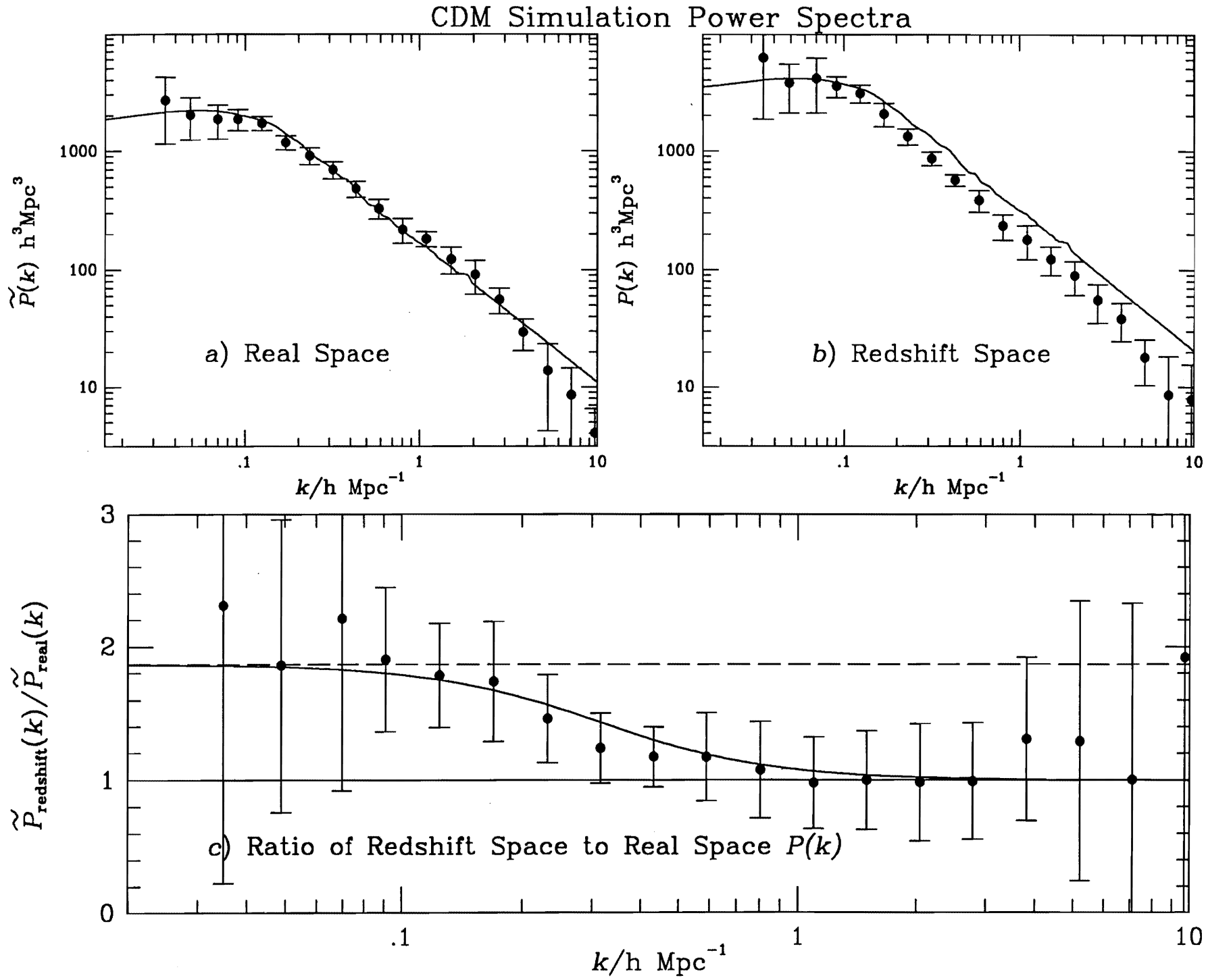
CDM Simulation Power Spectra
a) Real Space
b) Redshift Space
c) Ratio of Redshift Space to Real Space P(k)
$\tilde{P}(k)$ h^{3}Mpc^3
$P(k)$ h^{3}Mpc^3
$\tilde{P}_{redshift}(k)/\tilde{P}_{real}(k)$
k/h Mpc^{-1}
1000
100
10
.1
1
10
0
1
2
3

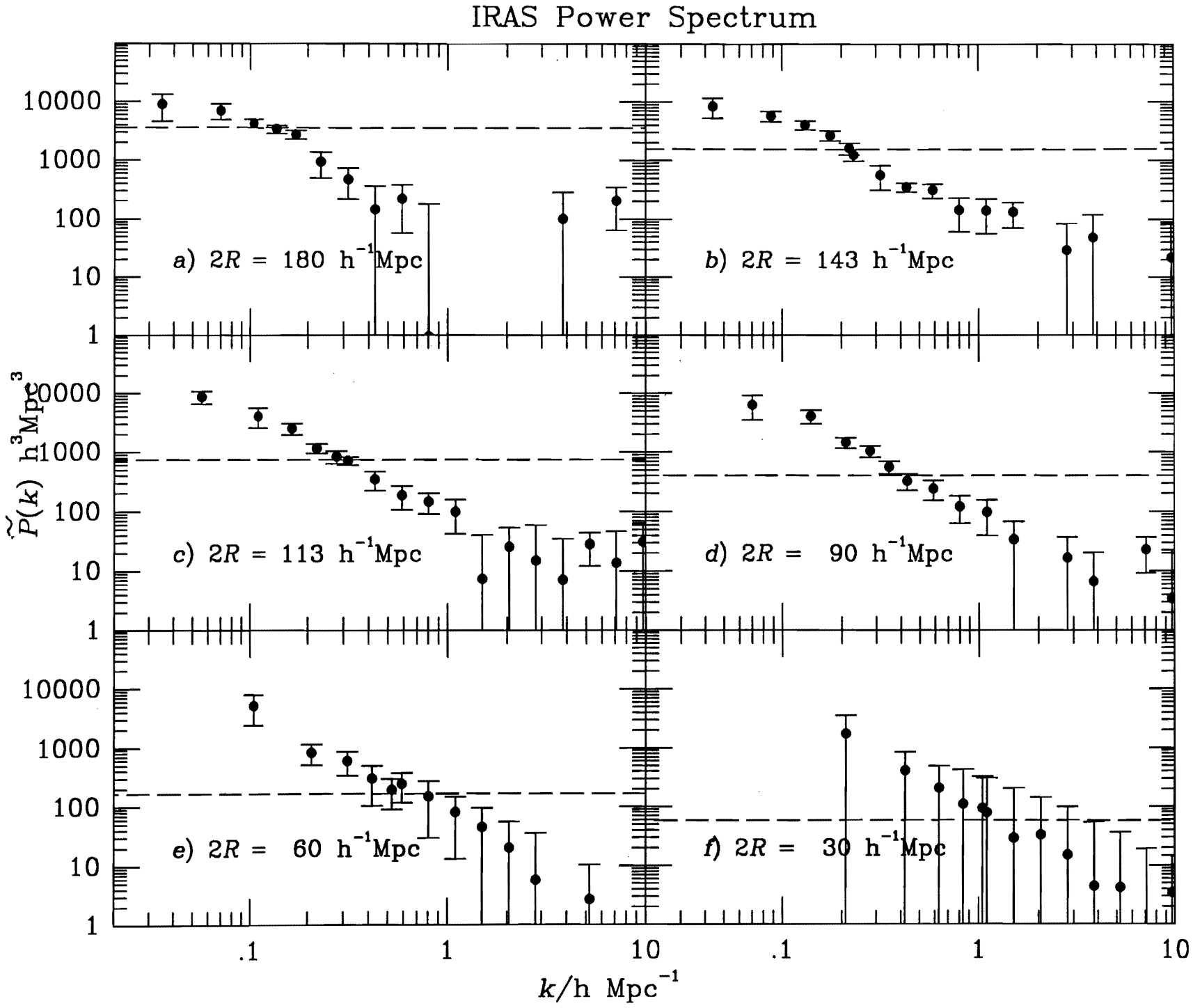
IRAS Power Spectrum
a) 2R = 180 h⁻¹Mpc
b) 2R = 143 h⁻¹Mpc
c) 2R = 113 h⁻¹Mpc
d) 2R = 90 h⁻¹Mpc
e) 2R = 60 h⁻¹Mpc
f) 2R = 30 h⁻¹Mpc
10000
1000
100
10
1
.1
1
10
P̃(k) h³Mpc³
k/h Mpc⁻¹

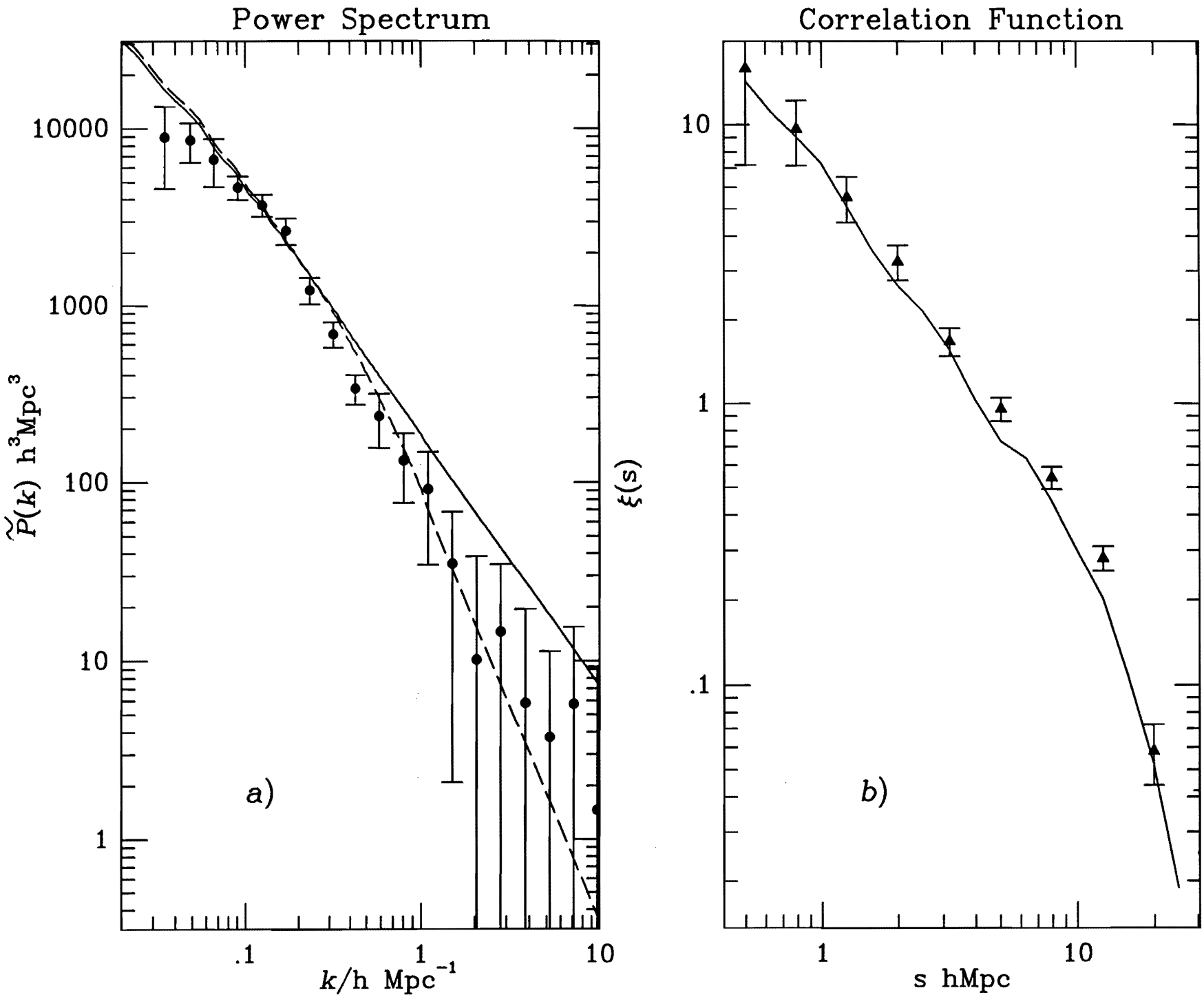
Power Spectrum
10000
1000
100
10
1
$\tilde{P}(k)$ h^{3}Mpc^3
a)
.1
1
10
k/h Mpc^{-1}
Correlation Function
10
1
.1
$\xi(s)$
b)
1
10
s hMpc

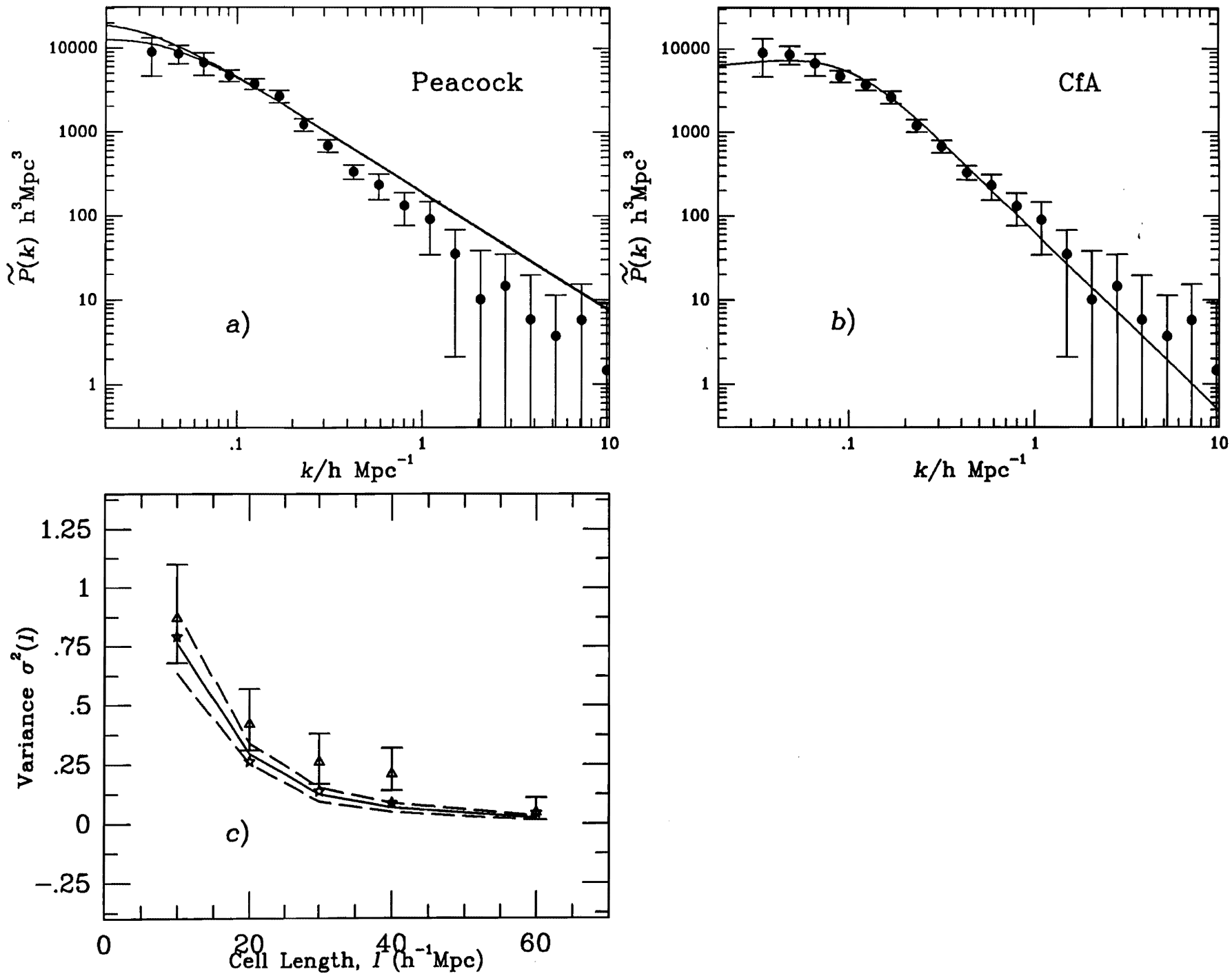
Peacock
a)
CfA
b)
c)
$\tilde{P}(k)$ h^{3}Mpc^3
k/h Mpc^{-1}
Variance $\sigma^2(l)$
Cell Length, l (h^{-1}Mpc)

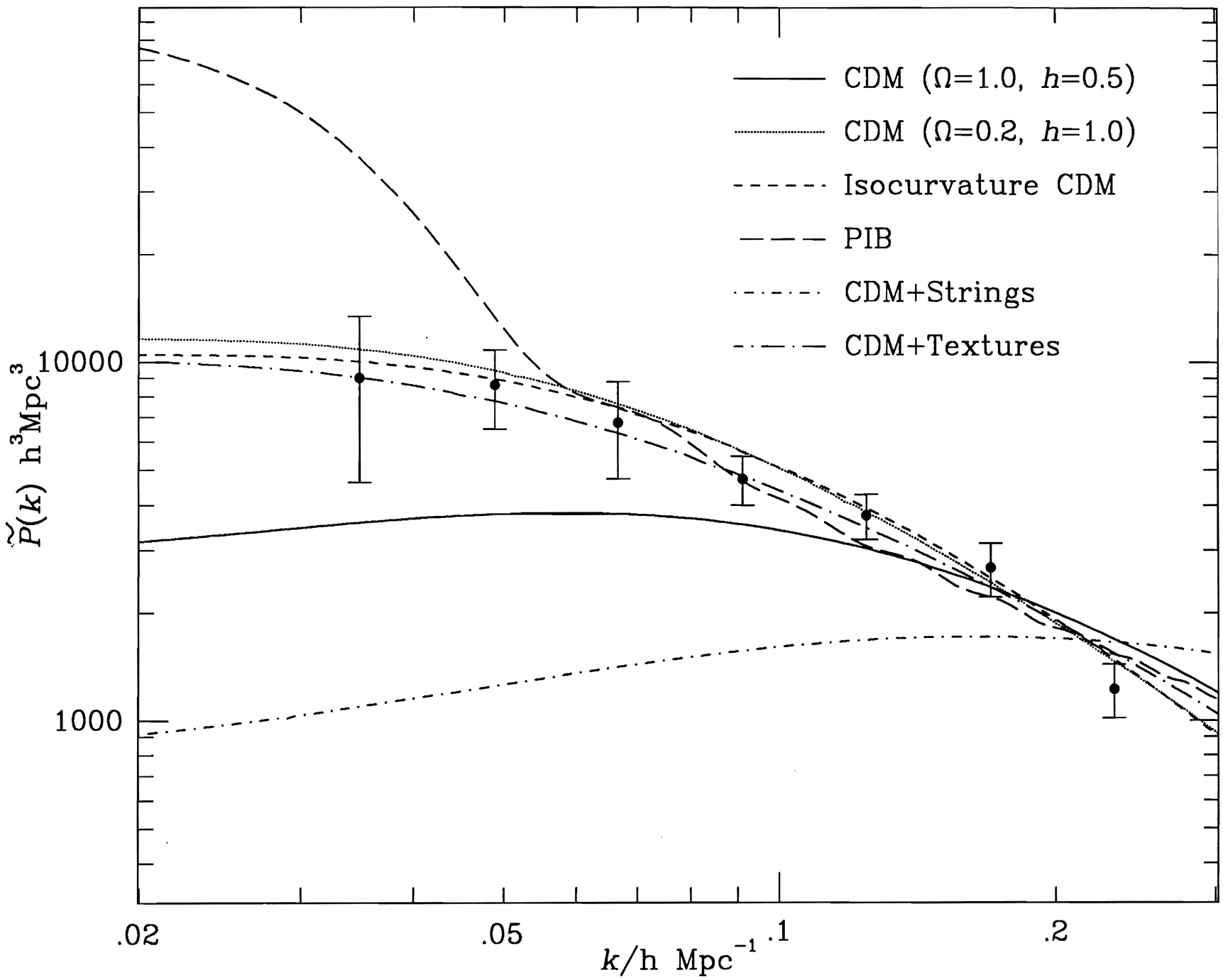
CDM (Ω=1.0, h=0.5)
CDM (Ω=0.2, h=1.0)
Isocurvature CDM
PIB
CDM+Strings
CDM+Textures
10000
1000
$\tilde{P}(k)$ h^{3}Mpc^3
.02
.05
.1
.2
k/h Mpc^{-1}

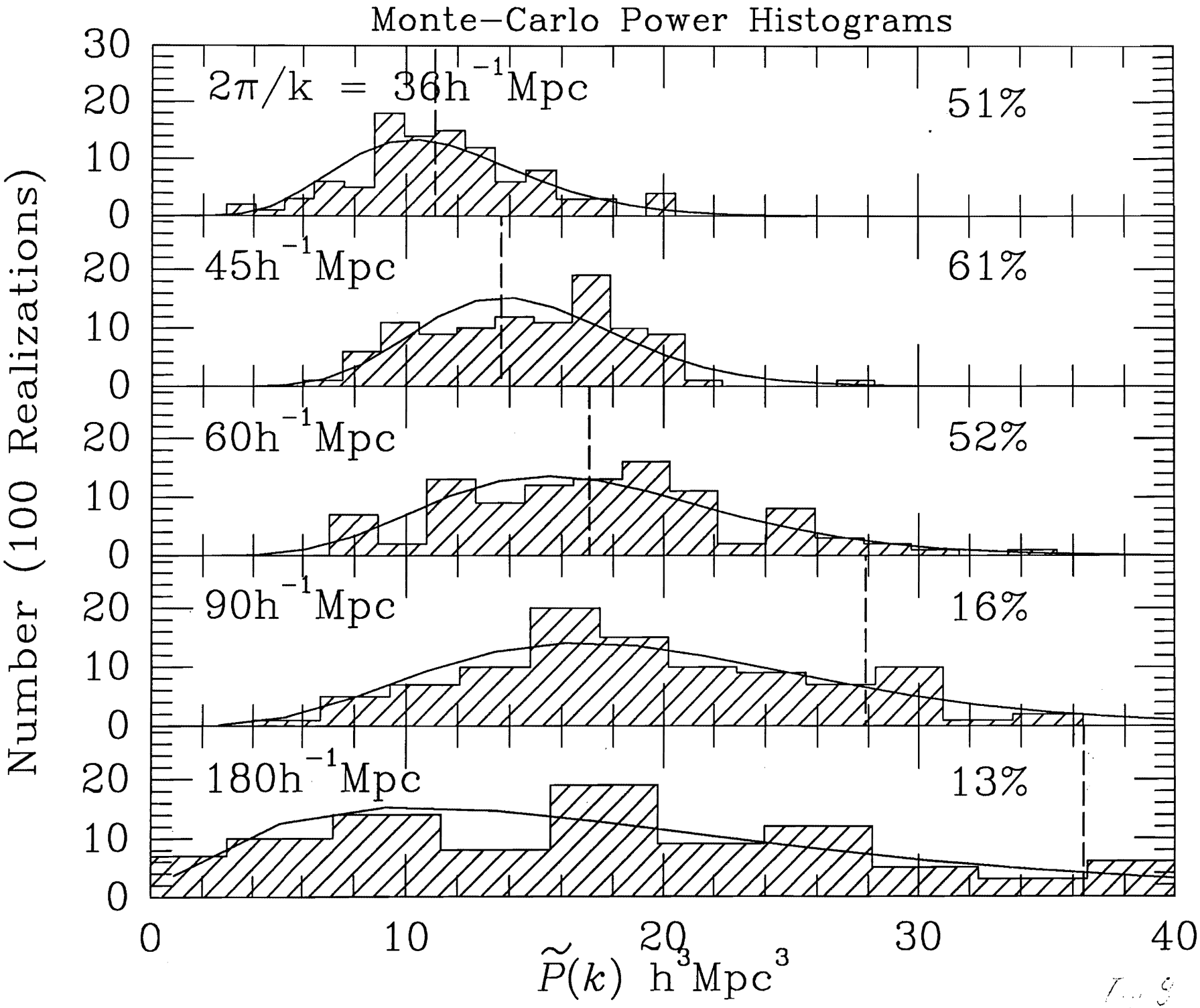
Monte−Carlo Power Histograms
2π/k = 36h⁻¹Mpc
51%
45h⁻¹Mpc
61%
60h⁻¹Mpc
52%
90h⁻¹Mpc
16%
180h⁻¹Mpc
13%
Number (100 Realizations)
0
10
20
30
0
10
20
30
40
P̃(k) h³Mpc³

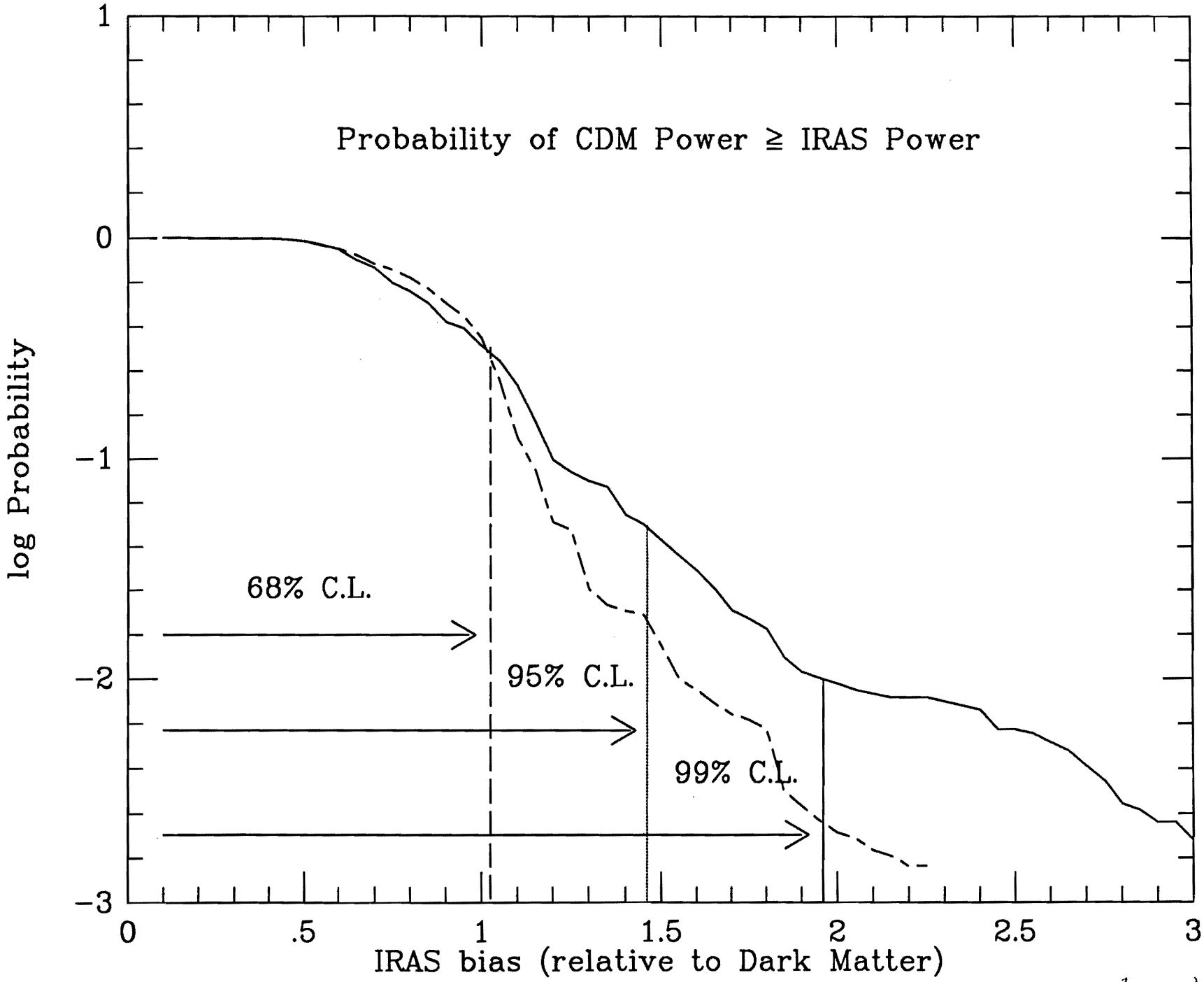
Probability of CDM Power ≧ IRAS Power
log Probability
IRAS bias (relative to Dark Matter)
68% C.L.
95% C.L.
99% C.L.
1
0
−1
−2
−3
0
.5
1
1.5
2
2.5
3

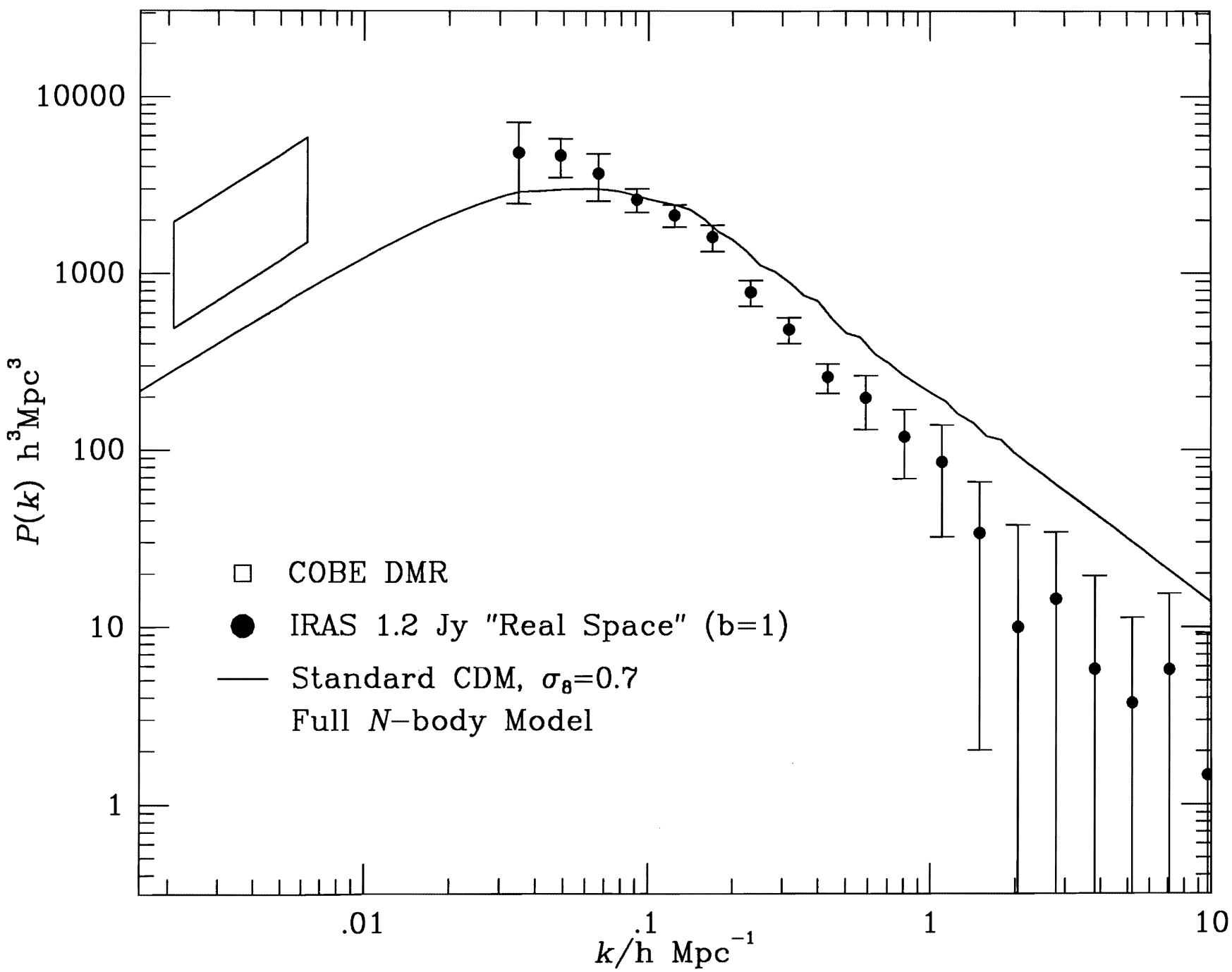
10000
1000
100
10
1
$P(k)$ $h^3 Mpc^3$
.01
.1
1
10
k/h Mpc^{-1}
COBE DMR
IRAS 1.2 Jy "Real Space" (b=1)
Standard CDM, σ_8=0.7
Full N-body Model